XMM-Newton

XMM-Newton Science Analysis System (version 6.5)

XMM-SOC-USR-TN-0009 Issue 2.1

M. Guainazzi, C.Gabriel, B.Altieri, I.Caballero, M.Ehle, J.Hoar,
M.G.F.Kirsch, A.Pollock, R.Saxton, M.Stühlinger, A.Talavera
XMM-Newton Science Operations Center

J.Osborne, C.Page, I.Stewart, M.Watson
XMM-Newton Science Survey Center

20 December 2005

Revision history

Revision number	Date	Revision author	Comments
0.1	29 January 2004	M.Guainazzi	LATEX template
0.2	5 March 2004	M.Guainazzi	First complete draft
0.3	15 March 2004	M.Guainazzi	Second complete draft (after SOC/SSC-LUX comments)
0.4	23 March 2004	M.Guainazzi	Third complete draft (after SOC/SSC comments)
1.0	24 March 2004	M.Guainazzi	Public version for SASv6.0
2.0	16 August 2005	M.Guainazzi	Public version for SASv6.5 (only EPIC part of the validation addressed)
2.1	20 December 2005	M.Guainazzi	Public version for SASv6.5

Contents

1 Introduction **1**
1.1 Concept . . . 1
1.2 Methodology . . . 1

2 EPIC camera imaging modes **3**
2.1 EPIC cameras effective area . . . 3
2.1.1 G21.5-0.9 . . . 3
2.1.2 PKS0558-504, Obs.#0125110101, Rev.#84 . . . 5
2.1.3 PKS0558-504, Obs.#0129360201, Rev.#153 . . . 6
2.2 MOS low sensitivity patch . . . 9
2.3 Response matrices for arbitrarily binned EPIC spectra . . . 12

3 EPIC-pn fast modes **13**
3.1 Her-X1–Validation of EPIC-pn Timing mode . . . 13
3.2 Crab – Validation of EPIC-pn Burst mode . . . 13
3.3 Relative timing of EPIC-pn . . . 15

4 OM **18**
4.1 SAS OM grism data processing . . . 18
4.1.1 Obs.#0125911301: HD 13499 . . . 18
4.1.2 Obs.#0125910901: HZ 2 . . . 20
4.2 SAS interactive tasks validation . . . 22
4.2.1 `omsource` . . . 22
4.2.2 `omgsource` . . . 22
4.3 Calibration items . . . 22
4.3.1 OM filter photometry . . . 22
4.3.2 OM astrometry . . . 25
4.3.3 OM grisms wavelength scale and flux calibration . . . 27
4.3.4 OM Fast Mode timing accuracy . . . 28

5 RGS **29**
5.1 Small but significant revision to the default behavior of `rgsproc` . . . 29
5.2 The use of `rgsfluxer` . . . 31
5.3 The RGS wavelength scale . . . 31
5.4 New RGS tasks in SAS v6.5 . . . 31
5.4.1 `rgscombine` . . . 31
5.4.2 `rgssuperrmf` . . . 33

6 Conclusions **33**

1 Introduction

1.1 Concept

Scientific Validation (SV) is required in order to ensure a constant high quality of the XMM-Newton Science Analysis System (SAS).
The main purpose of the SV is to provide the SAS community with a stable reliable software product, as well as to generate a list of caveats and known deficiencies. Together with these "functional" tests, the SV provides some information on the expected systematic uncertainties when basic data analysis products are generated through the current version of the SAS, using the best calibrations available at the moment SAS was released. It is important to stress that *this document does not supersede or substitute* the **instrument calibration status documents**, available from the XMM-Newton calibration portal. Instrument calibration is a continuous activity, whose results (update of calibration files) is intrinsically and necessarily decoupled from software releases. XMM-Newton users are recommended to consult periodically the URL: `http://xmm.vilspa.esa.es/calibrations`, which informs on the calibration status of the XMM-Newton instruments.
The document you are reading (*SAS Science Validation Report*) contains information about:

- which instrumental modes are fully supported by SAS,
- which scientific products SAS can produce,
- the level of accuracy associated with those products,
- a list of caveats and problems.

The SV is performed on a standard set of XMM-Newton observations, which cover all commissioned observational modes. Tab. 1 lists all the datasets used for the validation of SAS version 6.5 (*SAS v6.5* hereinafter). Some of these observations are particularly suitable to test calibration-related items, as specified in the rightmost column of Tab. 1. These datasets are intended as a standard reference, which has been and will be used to verify the performances of all SAS versions. However, additional datasets may occasionally be used to test version-specific SAS items. This is the case, for instance, for the datasets discussed in Sect. 2.2 of this report. Datasets discussed in a given report and not listed in Tab. 1 do not belong to the reference datasets, and are therefore not intended to be discussed in later SAS versions validation reports.

1.2 Methodology

The SV for SAS v6.5 consisted of the following steps:

1. the same datasets are also processed through the SAS reduction meta-tasks: `e[mp]proc`, `e[mp]chain`, `om[ifg]chain`, `rgsproc`
2. products generated by the above step were used as basis for the *interactive SV analysis*. Standard scientific products (images, light curves, spectra, source lists) are generated and analyzed. This allows to:
   - test the SAS interactive tasks.
   - verify the calibration accuracy obtained with SAS v6.5, and compare it with the expected accuracy on the basis of the calibration status at the time the SV is performed.

Table 1: SV datasets

Instrument	Mode	Object	Revolution Observation ID	Dataset ID	Calibration item
EPIC MOS	Full Frame	Lockman Hole	070 0123700101	1	Astrometry
	"	G21.5.09	060 0122700101	2	Effective area
	Small Window (W2)	Mkn 421	165 0099280201	3	
	Large Window (W3)	PKS0558-504	153 0129360201	4	Effective area
	Timing Uncompressed	Her X-1	207 0134120101	5	Timing
EPIC-pn	Full Frame	Lockman Hole	070 0123700101	1	Astrometry
	Full Frame/Small Window	PKS0558-504	153 0129360201	4	Effective area
	Large Window	AB Dor	185 0133120201	6	
	Small Window	PKS0558-504	084 0125110101	7	Effective area
	Fast Timing	Her X-1	207 0134120101	5	Timing
		Crab	411 0153750401	8	
	Fast Burst	Crab	411 0153750301	9	Timing
		Crab	411 0153750501	10	Timing
	Extended Full Frame	G21.5-0.9	060 0122700101	2	Effective area
RGS	SPEC+Q	PKS0558-504	084 0125110101	7	
"		Mkn 421	165 0099280201	3	Effective area
	"	AB Dor	185 0133120201	6	Wavelength scale
	"	AB Dor	338 0134521301	11	Wavelength scale
	"	AB Dor	462 0134521601	12	Wavelength scale
	"	AB Dor	572 0134522201	13	Wavelength scale
OM	Image Mode	BPM 16274	261 0125320701	14	Photometry
	Fast Mode	X1822-371	228 0111230101	15	
	FF Low Resolution	BPM 16274	261 0125320701	14	Astrometry
	Optical grism	Hz2	503 0125910901	16	Wavelength scale & flux calibration
	UV Grism	HD13499 (offset)	657 0125911301	17	Wavelength scale & flux calibration

Table 2: Best-fit parameters and results when a photoelectrically absorbed power-law model is applied to the EPIC spectra of G21.5-0.9

Camera	N_H (10^{22} cm^{-2})	Γ	2-10 keV flux (10^{-11} cgs)
MOS1	2.16 ± 0.04	1.85 ± 0.03	6.13 ± 0.05
MOS2	2.16 ± 0.04	1.90 ± 0.03	5.91 ± 0.05
pn	2.13 ± 0.03	1.856 ± 0.016	6.16 ± 0.03

The conclusions of the SV are summarized in Sect. 6. A list of instrument modes supported by SAS v6.5 is reported in Appendix A. A summary of SAS v6.5 capabilities is detailed in Appendix B.
In this report: best-fit parameter uncertainties are at the 90% confidence level for 1 interesting parameter ($\Delta\chi^2 = 2.71$); errors on positions or count rates are at the 1-σ level; energies are quoted in the observer's reference frame unless otherwise specified.

2 EPIC camera imaging modes

2.1 EPIC cameras effective area

2.1.1 G21.5-0.9

The X-ray spectrum of the Crab-like SuperNova Remnant (SNR) G21.5-0.9 (Warwick et al. 2001) is well described by a strongly absorbed (column density, $N_H \sim 2 \times 10^{22}$ cm^{-2}) power-law. At 0-th order, it can be characterized through 3 quantities only: N_H, the photon index Γ and the model normalization or flux. This source is therefore particularly well-suited to compare the performances of the response matrices above 1 keV.
The XMM-Newton observation discussed in this report was performed on April 7, 2000. The EPIC cameras were operating in Full Frame (MOS), and Extended Full Frame (pn) mode, respectively. The source was on-axis. Data were reduced with both the `chain`s and the `proc`s EPIC reduction meta-tasks. Although the resulting event lists are not completely identical due to residual small infrastructure differences, we have verified that the spectral results described hereafter are indistinguishable at the last significant digits.
Source spectra were extracted from circular regions of $2.7'$ radius around the centroid of the SNR. Background spectra were extracted from annuli of $3.15'$ to $4.6'$ radius. The source spectra were rebinned in order to have at least 50 counts in each spectral bin and to oversample the instrumental energy resolution by a factor not higher than 3. The spectra were fit in the 0.5-10 keV and 0.3-10 keV energy bands for MOS and p-n, respectively. Effective areas were generated using exposure-specific detector maps, as recommended for extended sources. As already stressed in the SASv6.0 Science Validation Report, wrong results are obtained, if one uses a *flat* detector map in either `arfgen` or `rmfgen`.
The best-fit results are shown in Tab. 2 and Fig. 1, and Fig. 2. Residuals are within $\pm 5\%$ across the whole sensitive bandpass of the EPIC cameras. The MOS 2 cameras exhibits a steeper spectrum ($\Delta\Gamma \lesssim 0.05$), and a lower 2–10 keV flux by $\simeq 4\%$. Otherwise, the best-fit parameters are basically consistent within the statistical uncertainties. The difference between the results in the MOS2 and in the other cameras may be related to a $\simeq 1'$ shift between the nominal boresight position and the optical axis, which is still not perfectly accounted for by the response matrices

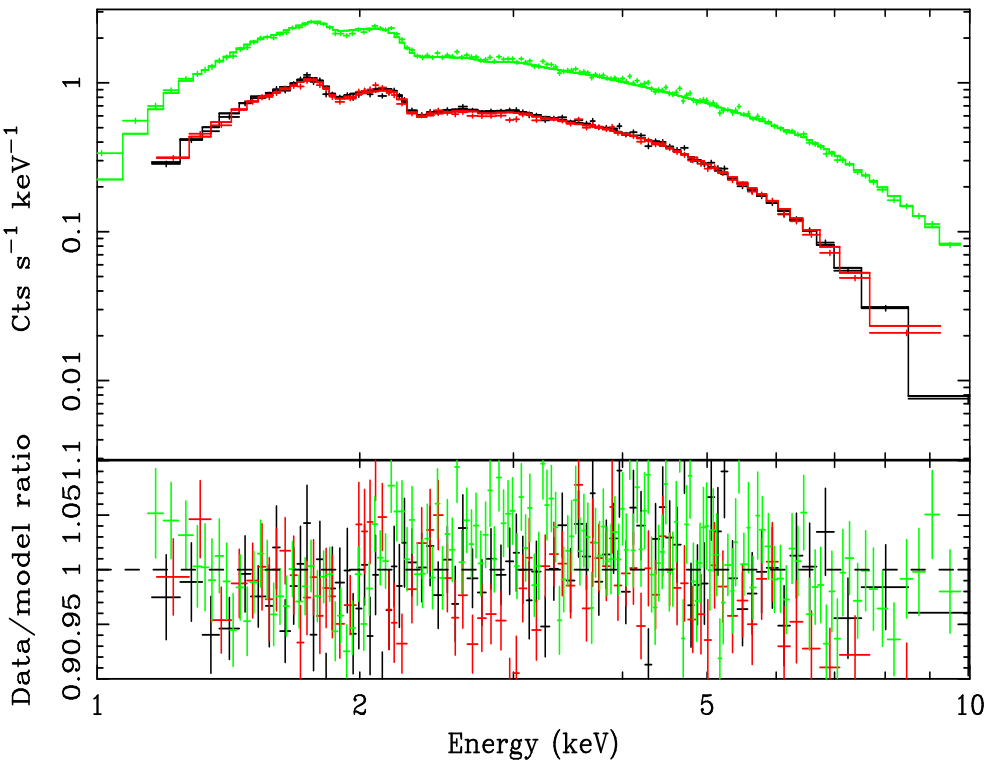

Figure 1: EPIC spectra (*upper panel*) and residuals in units of data/model ratio (*lower panel*), for the spectral fit in Tab. 2; MOS1: *black*; MOS 2: *red*; pn *green*. Each data point corresponds to a signal-to-noise ratio $\geq$25.

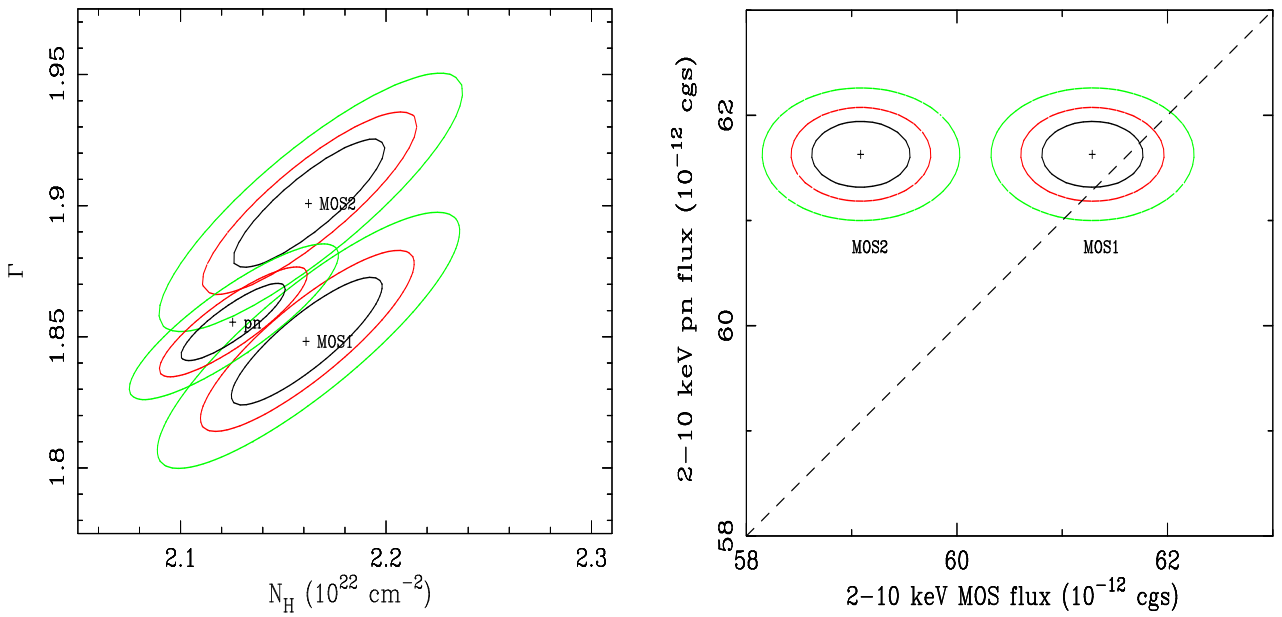

Figure 2: *Left panel*: iso-χ^2 contour plots for N_H versus Γ. Contours are at 68%, 90%, and 99% confidence levels for two interesting parameters. *Right panel*: iso-χ^2 contour plots for the MOS 2–10 keV observed flux versus the pn flux in the same energy band. The *dashed line* indicates the locus of equal fluxes

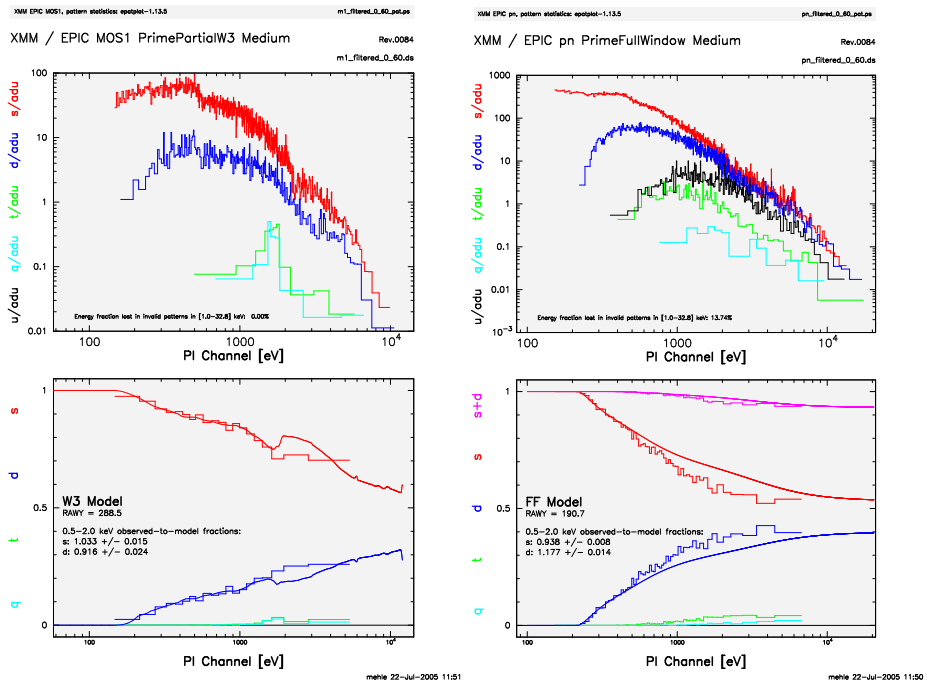

Figure 3: The `epatplot` output for circular extraction regions about PKS0558-504 for MOS-1 (`left`) and pn (`right`) in Rev.#84 (*i.e.*, before excising of the PSF core)

averaging.

2.1.2 PKS0558-504, Obs.#0125110101, Rev.#84

Here we analyze the first exposure of the Rev.#84 observation of PKS0558-504 made with the pn detector in Full Frame mode and the two MOS cameras in Large Window mode. All of the cameras use the medium filter and suffer from a modest amount of pile-up (the count-rate is 14.0 s^{-1} for pn, and 6.2 s^{-1} for the MOS cameras).
Spectra were initially extracted from circular regions centered on the source using `especget` and were tested for pile-up using `epatplot`. All of the plots show significant deviation from the expected pattern fraction curves (Fig. 3) and it was necessary to exclude the inner 5″ and 10″ from the MOS and pn extraction regions, respectively to get good agreement with the model[1]. The pn data were screened for high flaring background, resulting in an exposure time of 4.7 ks. These time intervals were used to extract events for all the three cameras to ensure that source variability would not affect the comparison of the camera spectra. Spectra were extracted from annuli of 5–60 (MOS) and 10–60 (pn) arc-seconds about the source with the pn time windows and standard selections of (`FLAG==0 && PATTERN<=4`) (pn) and (`#XMMEA_EM && PATTERN<=12`) (MOS) applied. Background spectra were extracted from source-free areas of sky near to the target and response matrices were created using `arfgen` and `rmfgen` in the standard manner. The source spectra were grouped to give a minimum number of 25 counts per channel and a factor of three by which to oversample the EPIC energy resolution and were fit independently

[1] Users may refer to XMM-NEWS#31 (`http://xmm.vilspa.esa.es/external/xmm_news/news_list/xmm_news-2003-03-27.shtml`) for a discussion on this analysis approach

Table 3: Rev.#84 PKS0558-504 best-fit parameters for a power-law plus two black-body model with the hotter black-body having a fixed temperature of 150 eV. kT and N_{BB} are the temperature and normalization of the black-body components. F is the measured flux.

Instrument	Γ	kT^1_{BB} (eV)	N^1_{BB} 10^{-5}	kT^2_{BB} (eV)	N^2_{BB} 10^{-6}	F (0.2–2 keV) (10^{-11} erg cm^{-2} s^{-1})	F (2–10 keV)	χ^2/dof
pn	$2.26\pm^{0.08}_{0.07}$	67 ± 4	29 ± 4	150	$96\pm^{16}_{19}$	2.15	0.80	109/129
MOS1	$2.16\pm^{0.10}_{0.09}$	$62\pm^{5}_{4}$	$40\pm^{8}_{7}$	150	$93\pm^{20}_{23}$	2.15	0.89	121/118
MOS2	$2.18\pm^{0.10}_{0.09}$	58 ± 4	$45\pm^{11}_{7}$	150	96 ± 21	2.20	0.90	132/117

with a model constituted by a power-law and two black-bodies attenuated by absorption in cold gas fixed at the measured galactic value of 4.4×10^{20}cm^{-2} (O'Brien et al. 2001). The hotter black-body temperature was poorly constrained and so was fixed at 150 eV in the fits. The best-fit parameters are given in Table 3. The fits for the three EPIC cameras are seen to be in good agreement and the fluxes are very similar: at low energies derived fluxes agree within within the errors. In the 2–10 keV band, the measured pn flux was found to be $\sim 10\%$ lower than the MOS flux.
The best fits and residuals are presented for the three cameras in Fig. 4.

2.1.3 PKS0558-504, Obs.#0129360201, Rev.#153

Here we analyze the EPIC observations obtained in Rev.#153: a pn exposure was performed in Small Window mode and MOS1 and MOS2 in Large Window mode with the Thin1 filter in place for all these exposures. The ODF was processed with the `epproc` and `emproc` tasks to generate MOS and pn calibrated event lists.
The exposures were free of flaring background and the total 10.7 ks (pn) and 7.9 ks (MOS) could be taken into account.
According to the `epatplot` created pattern statistics (Fig. 5), the EPIC window mode observations are not significantly affected by pile-up. This holds especially true for the pn Small Window exposure whereas there might be some marginal deviations of the MOS data from the model. The pn Full Frame mode exposures also taken in Rev.#153 are strongly affected by pile-up, and therefore were excluded from this report.
Checking the light curves of PKS0558-504 obtained during the EPIC partial window observations (Fig. 6), the source was found to be variable. The further analysis of the spectra obtained with the three different EPIC cameras therefore was restricted to the time interval in which all instruments were simultaneously collecting data. This reduced the effective exposure time to 7.0 ks. We used `xmmselect` to display the EPIC data in sky coordinates and to define source and background regions for `especget`: Source spectra have been extracted from circular areas centered on PKS0558-504 and background spectra from source-free rectangular regions from the same CCD. Standard quality flag and pattern selections, as defined in `especget`, have been adopted: `((FLAG==0) && (PATTERN<=4))` (pn) and `(#XMMEA_EM && (PATTERN<=12))` (MOS). Response matrices have been generated on the fly by `especget` calling `rmfgen` and `arfgen`, with `detmaptype=psf`.
Source spectra have finally been grouped with a minimum number of 25 counts per channel and a factor of three by which to oversample the EPIC energy resolution.

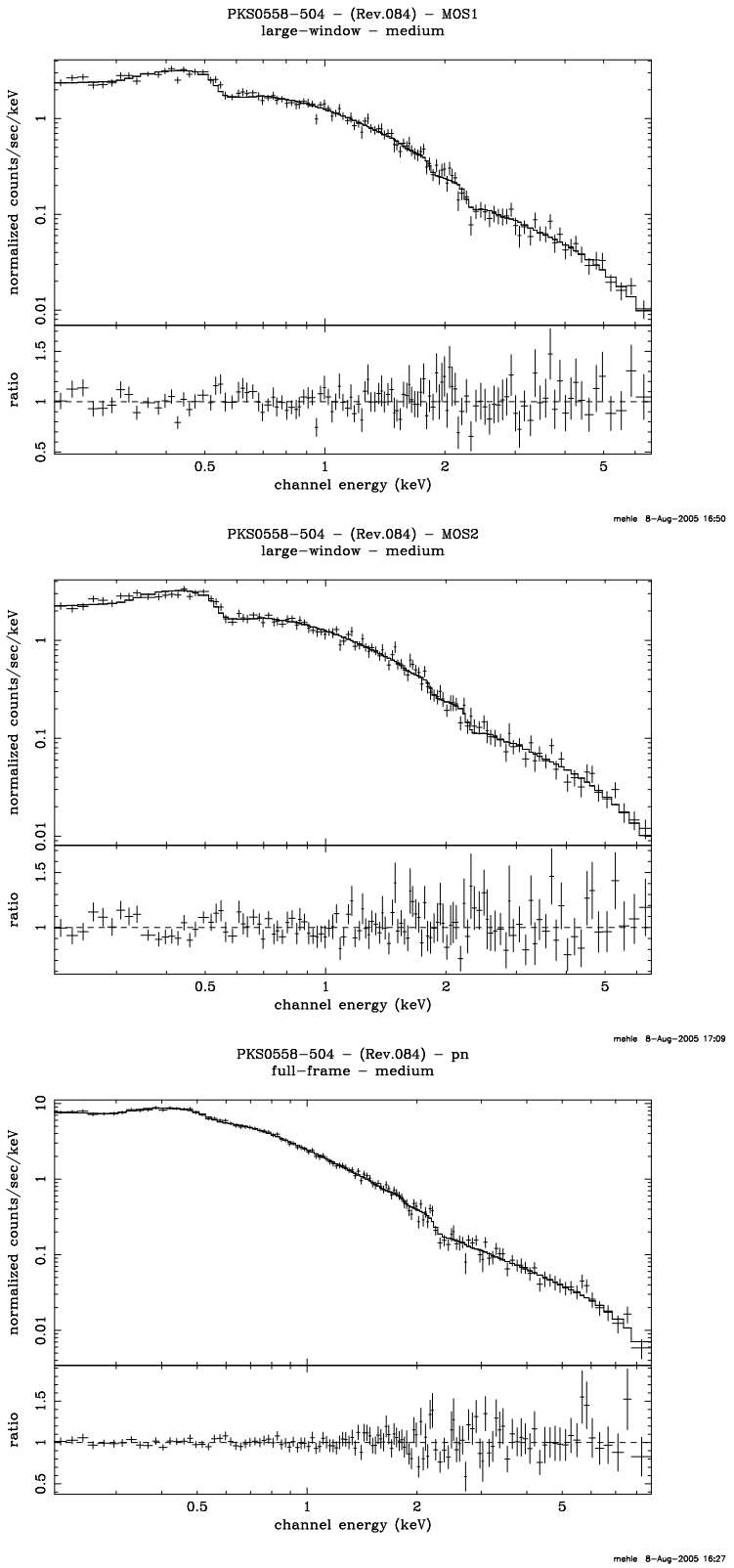

Figure 4: Spectra and residuals for MOS1 (*upper*), MOS2 (*middle*) and pn (*lower*) fits to the Rev.#84 observation of PKS0558-504 (after excision of the PSF core)

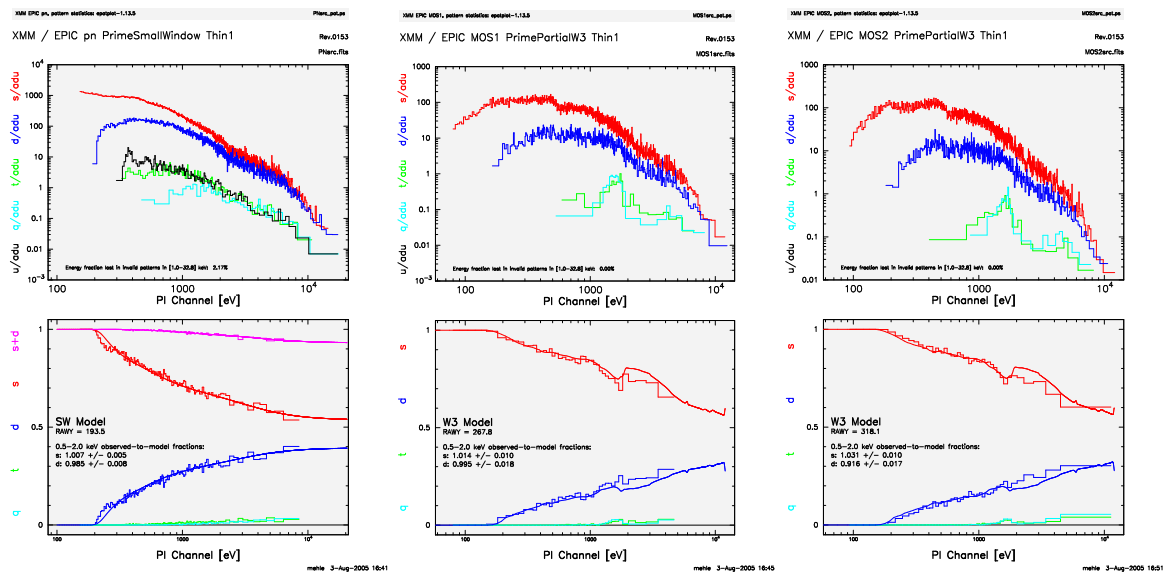

Figure 5: PKS0558-504 pattern statistics of the pn Small Window (*left panel*), and the MOS1 and MOS2 Large Window (*middle & right panel*) exposures in Rev.#153, produced by the SAS task `epatplot`.

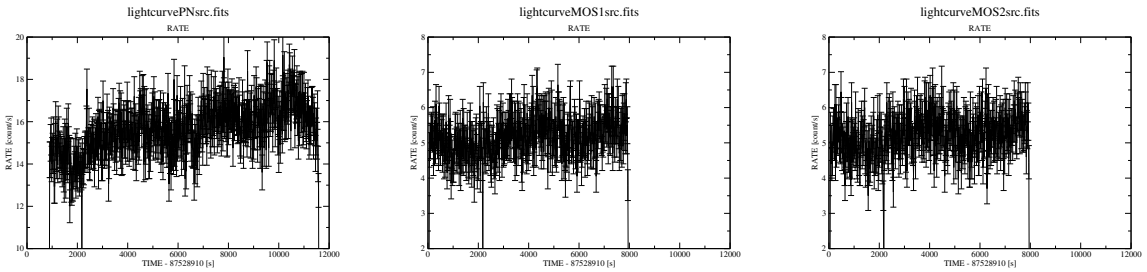

Figure 6: PKS0558-504 light curves of the pn Small Window (*right panel*), and the MOS1 and MOS2 Large Window (*center & left panel*) exposures in Rev.#153. The bin-size is 20 s and the energy selection 0.15-10 keV.

Table 4: PKS0558-504 best-fit parameters for pn Small Window mode and MOS Large Window mode observations in Rev.#153. N are the normalizations and kT the temperatures of the blackbody components. F is the measured model flux.

	Γ	N_Γ (10^{-4})	kT^1_{BB} (eV)	N^1_{BB} (10^{-5})	kT^2_{BB} (eV)	N^2_{BB} (10^{-6})	F(0.2-2 keV) (10^{-11} erg cm^{-2} s^{-1})	F(2-10 keV)	χ^2/ dof
pn	2.18 ± 0.04	$59\pm^{2}_{3}$	53 ± 3	37 ± 5	$142\pm^{7}_{6}$	139 ± 10	2.53	1.17	183/197
MOS1	2.19 ± 0.07	61 ± 4	$56\pm^{3}_{6}$	$35\pm^{8}_{10}$	$146\pm^{14}_{15}$	$94\pm^{16}_{17}$	2.41	1.17	152/165
MOS2	$2.25\pm^{0.07}_{0.06}$	67 ± 4	$58\pm^{6}_{12}$	$23\pm^{38}_{6}$	$128\pm^{19}_{16}$	$97\pm^{41}_{15}$	2.43	1.20	137/166

Table 5: PKS0558-504 best-fit parameters of simultaneous pn, MOS1 and MOS2 data fitting. N are the normalizations and kT the temperatures of the blackbody components. C marks the fit constants for pn/MOS1/MOS2, respectively, and F the model flux for pn.

Γ	N_Γ (10^{-4})	kT^1_{BB} (eV)	N^1_{BB} (10^{-5})	kT^2_{BB} (eV)	N^2_{BB} (10^{-6})	C (%)	F(0.2-2 keV) (pn, 10^{-11} erg cm^{-2} s^{-1})	F(2-10 keV)	χ^2/ dof
$2.20\pm^{0.04}_{0.03}$	$62\pm^{23}_{18}$	55 ± 2	$34\pm^{5}_{3}$	$141\pm^{5}_{8}$	$120\pm^{11}_{7}$	100/95/97	2.52	1.20	540/526

The pn, MOS1 and MOS2 spectra have been fit individually with a model constituted of a power-law and two blackbody components all affected by foreground absorption fixed at the Galactic value of 4.4×10^{20} cm^{-2} (*baseline model*; the third blackbody envisaged by O'Brien et al. (2001) is actually not required by the fit of this dataset).
The power-law component dominates above 2 keV, the blackbodies account for the bulk of the prominent soft X-ray excess. The spectra and best-fit models are shown in Fig. 7, together with the data/model ratio residuals. Best-fit parameters and results are summarized in Tab. 4. The fits for the individual EPIC cameras (pn, MOS1 and MOS2) agree well (cf. Table 4). We note that the fit parameters to the MOS2 spectrum show somewhat larger errors than the ones for the pn and MOS1.
We found flux differences between pn and MOS of the order of 5% in the soft energy range 0.2 - 2 keV (where systematic fit residuals are found - cf. Fig. 8), whereas fluxes agree to better than 3% in the energy band 2 - 10 keV.
In addition to the camera specific fits, a simultaneous fit of pn, MOS1 and MOS2 Rev.#153 data using the baseline model was performed between 0.2 and 10 keV (see the left panel of Fig. 8). A constant factor was introduced to account for absolute flux discrepancies between the individual EPIC cameras: the factor was fixed to 100% for pn and let a free parameter for the two MOS. The residuals (cf. the right panel of Fig. 8) show that a general good agreement between the cameras is achieved: the discrepancy in the cross calibration of the EPIC instruments for this source, modes and filter are less than 10% in the ratio data/model. The discrepancies are somewhat larger around the 1.8 keV Si-edge. For completion the best fit parameters obtained are given in Tab. 5.

2.2 MOS low sensitivity patch

In this Section, the pn/MOS flux consistency on a recent observation is verified, after the discovery of a low sensitivity patch close to the MOS boresight and a hot column in MOS1

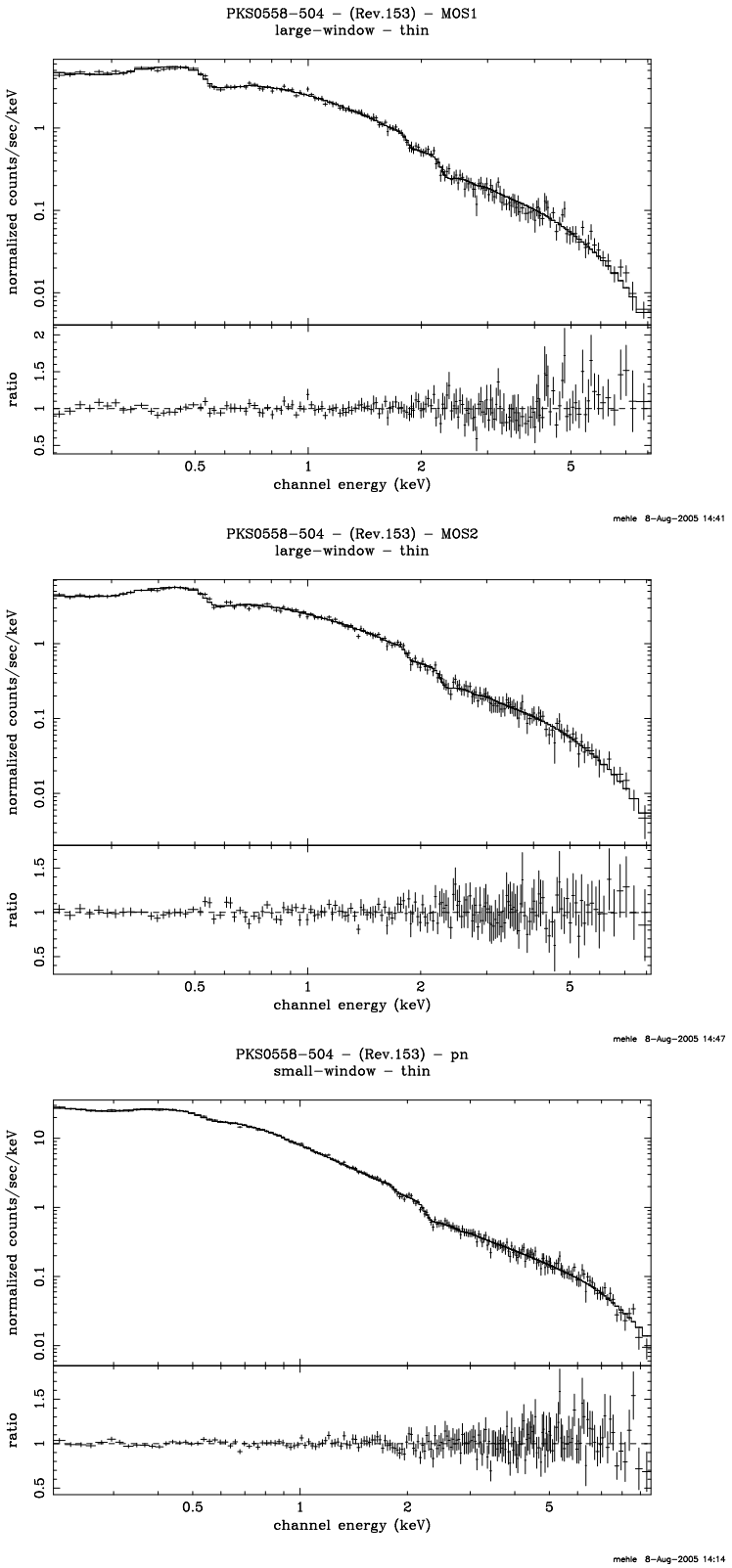

Figure 7: PKS0558-504 MOS1 (*top*), MOS2 (*top center*) and pn (*bottom*) spectra (*upper panel*) and residuals in units of data/model ratio (*lower panel*) when the baseline model is applied to the spectrum of the Large Window exposure in Rev.#.153.

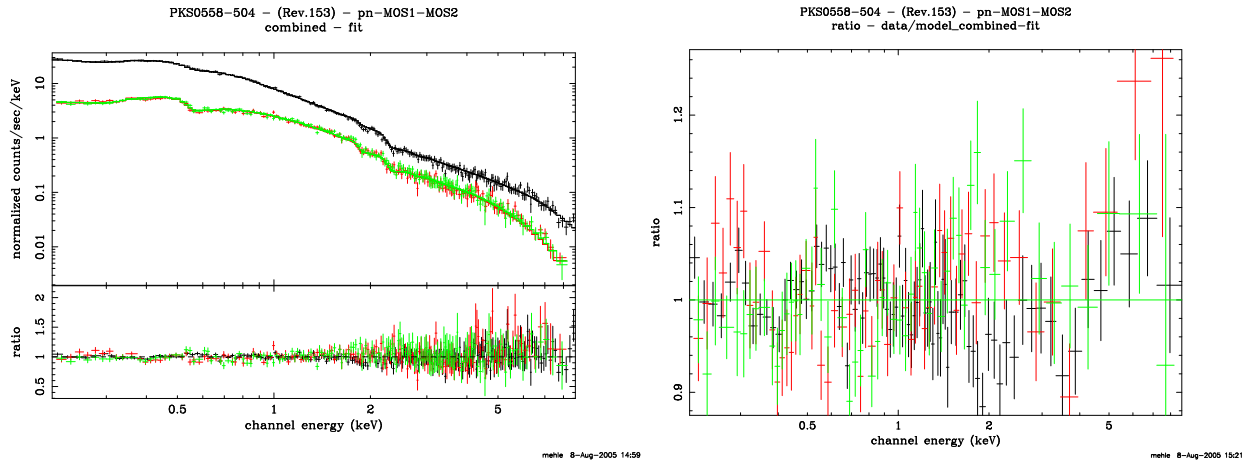

Figure 8: *Left panel*: PKS0558-504 pn (black), MOS1 (red) and MOS2 (green) spectra together with residuals in units of data/model ratio (*lower panel*) when the baseline model with additional factors for the three cameras is simultaneously applied to the spectra of the Small Window (pn) and Large Window (MOS) exposures of Rev.#153. *Right panel*: PKS0558-504 pn (black), MOS1 (red) and MOS2 (green) combined fit residuals in units of data/model ratio. Data were re-binned for clarity and plotting purposes.

Table 6: MOS/pn normalization constants for the fit of the Rev.#1012 observation of H1426+428. Statistical errors are ≃0.05.

	SASv6.1	SAS v6.5
MOS2 (`FLAG==0`)	0.98	1.02
MOS1 (`FLAG==0`)	0.89	0.98
MOS2 (`#XMMEA_EM`)	1.00	1.02
MOS1 (`#XMMEA_EM`)	0.96	0.99

CCD1. The tests have been performed on an observation of the blazar H1426+428 performed in Rev.#1012. During this observation a hot column was detected in the central MOS1 CCD, 9 pixels away from PSF center.
Spectra were Extracted for PN (`FLAG==0`), MOS2/1 (`FLAG==0` and `#XMMEA_EM`) for SAS 6.1 and SAS6.5. Using `FLAG==0`, three columns, the hot column plus adjacent columns, are ignored. Using `#XMMEA_EM`, only the hot column is ignored. The used fit model was a simple photoelectrically absorbed (Wilms' et al. (2000) abundances) power-law. The absorber column density was fixed to $N_H = 1.36 \times 10^{20}$ cm^{-2}. This model describes the data sufficiently well, to allow us to investigate the differences in flux and spectral shape between the spectra of the two SAS versions. Combined fits were performed, including normalization constants with PN fixed to 1.0. The results are summarized in Tab. 6. `arfgen` takes now properly into account the flux lost due the ignored columns. Using SAS6.1, MOS1 disagreed up to 11% for `FLAG==0` (3 columns were ignored). Using SAS6.5, MOS and PN agree within ±2% independent of the employed flags. (see Fig. 9). Differences are within about ±10% across the whole sensitive bandpass.
However, users are recommended to exercise caution when analyzing and interpreting data,

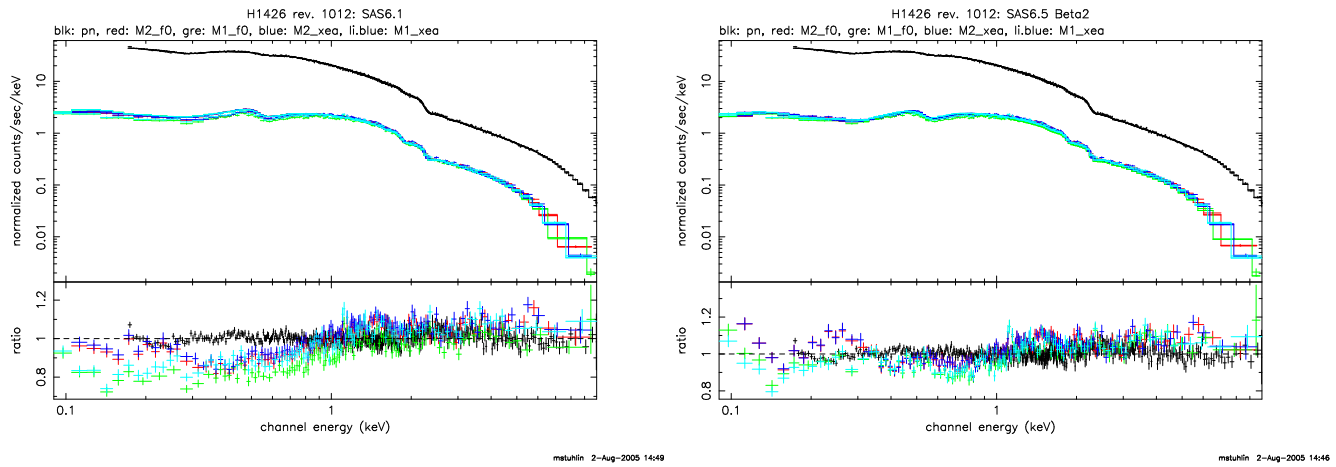

Figure 9: Comparison of the quality of spectral fitting among the EPIC camera when the H1426+428 data are reduced with SASv6.1 (*left panel*) and SASv6.5 (*right panel*)

Table 7: MOS/pn normalization constants for the fit of the observation of RXJ1856 (Obs.#0165971901), with respect to the MOS2 spectrum extracted with `#XMMEA_EM`

MOS2 (`FLAG==0`)	$1.022\pm^{0.014}_{0.008}$
MOS1 (`#XMMEA_EM`)	$0.651\pm^{0.012}_{0.006}$
MOS1 (`FLAG==0`)	$0.765\pm^{0.015}_{0.006}$

when hot columns are located 1 or 2 pixels away from the PSF center. This occurs, for instance, in a recent observation of RXJ 1856 (Obs.#0165971901). The adjacent columns to the hot one show a strong decrease of counts, but are not flagged as bad by `embadpixfind`. Using SAS6.1, these columns were flagged as bad. This leads to the extraction of a wrong MOS spectrum even if `#XMMEA_EM` is used, as adjacent columns are taken into account, and the PSF center is not clearly defined. In this case, it is advisable to use `FLAG==0` for the extraction of the spectra, which leads to ignoring adjacent columns. Still the results are not satisfactory (Tab. 7). This is probably due to the still incorrect determination of the PSF centroid.

2.3 Response matrices for arbitrarily binned EPIC spectra

As of SAS v6.5, one can generate response files for arbitrarily binned MOS spectra, as long as the binning is linear in the original channels. This means that users can set the `ev/xmmselect` parameter `spectralbinsize` to any value. We have tested that the spectral fit results are indistinguishable, when different spectral bin sizes are applied in the extraction of G21.5-0.9 spectra. The extension to pn spectra will be included in a future SAS version.

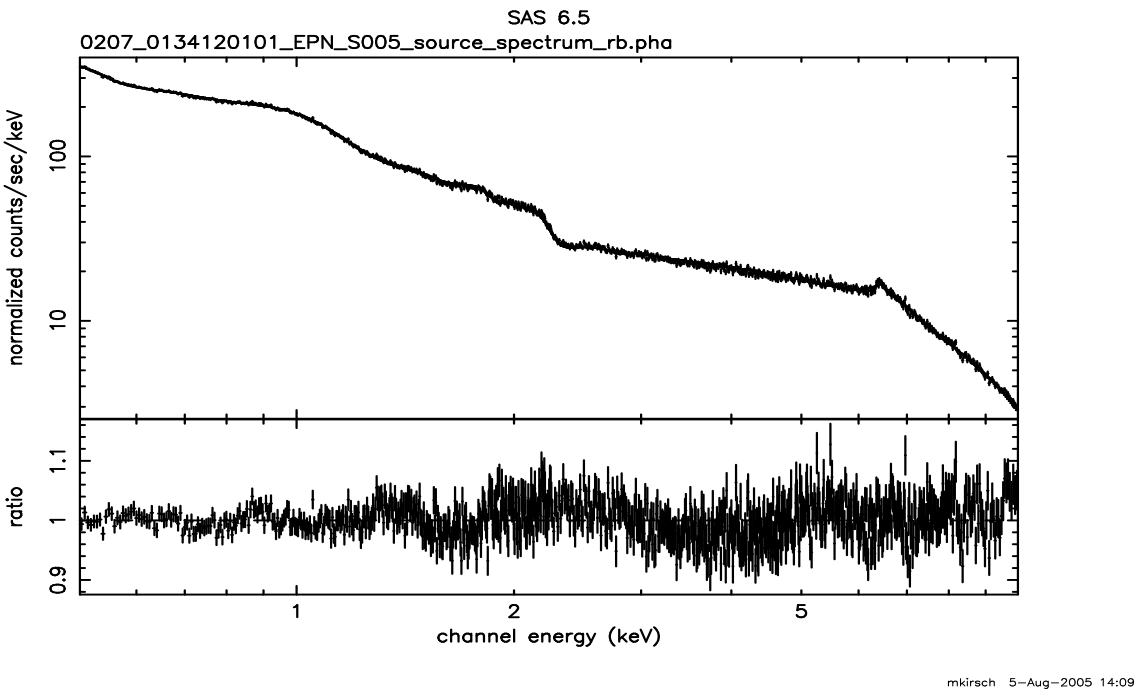

Figure 10: Spectrum of Her-X1 in EPIC pn Timing mode

3 EPIC-pn fast modes

3.1 Her-X1–Validation of EPIC-pn Timing mode

XMM-Newton observed Her-X1 ($\alpha_{2000} = 16^h57^m49^s.80$, $\delta_{2000} = +35°20'32''.6$) , several times. The observation used in this report took place on January 26, 2001, Rev.#207, lasting more than 9000 seconds.

For this analysis only EPIC-pn data have been used. We used the following setting to extract source and background regions, respectively: `((RAWX,RAWY) IN box(36.5,100,25,99.5,0))`, `((RAWX,RAWY) IN box(5,100.75,4.5,99.25,0))` Spectra have than been extracted using single and double events neglecting the events at CCD borders and events lower than 0.5 keV where data should not be used due to the high noise below 0.5 keV in EPIC-pn Timing Mode.

All response files have been created using SAS 6.5. The spectra have been fit with a model constituted by photoelectric absorption (the `wabs` implementation in XSPEC was used), a power-law, a disk blackbody, and four Gaussian lines (two of them intrinsically broad). Several residual features are known to be due to current uncertainties in the calibration. Fig. 10 shows a plot of Her-X1 (data and model) of the best fit to the EPIC-pn Timing mode spectrum. The best-fit parameters and results are summarized in Tab. 8.

3.2 Crab – Validation of EPIC-pn Burst mode

XMM-Newton observed the Crab Nebula ($\alpha_{2000} = 05^h34^m31^s.97$, $\delta_{2000} = +22°00'52''.1$) - encompassing the most famous pulsar of X-ray astronomy (Kirsch et al. 2005) - in Rev.#234, 411, 698, 700, 874 and 955 using the EPIC-pn-fast modes (*i.e.* Timing and Burst Modes). For spectral analysis only Burst mode data of the Crab are useful, since the spectra will be piled-up in Timing mode. However the Timing mode observations can be used for timing analy-

Table 8: Her-X1 best-fit parameters. The 0.5 keV Gaussian and the sigma of one iron line have been frozen. E_i^C indicates the centroid energy of the i-th line, σ_i its intrinsic width

χ^2/ dof	Γ	Tin [eV]	N_{BB} [10^4]	E_1^C [keV]	σ_1 [keV]	E_2^C [keV]	σ_2 [keV]
1215.0/848	$0.861\ \pm^{0.006}_{0.004}$	$177\ \pm^{5}_{7}$	$1.52\ \pm^{0.4}_{0.2}$	$0.5^{\dagger}$	$0.005^{\dagger}$	$0.9626\ \pm^{0.032}_{0.037}$	$0.143\ \pm^{0.004}_{0.002}$
				E_3^C [keV]	σ_3 [keV]	E_4^C [keV]	σ_4 [keV]
				$6.564\ \pm^{0.029}_{0.027}$	$0.436\ \pm^{0.052}_{0.045}$	$6.435\ \pm^{0.011}_{0.016}$	$0.005^{\dagger}$

†frozen

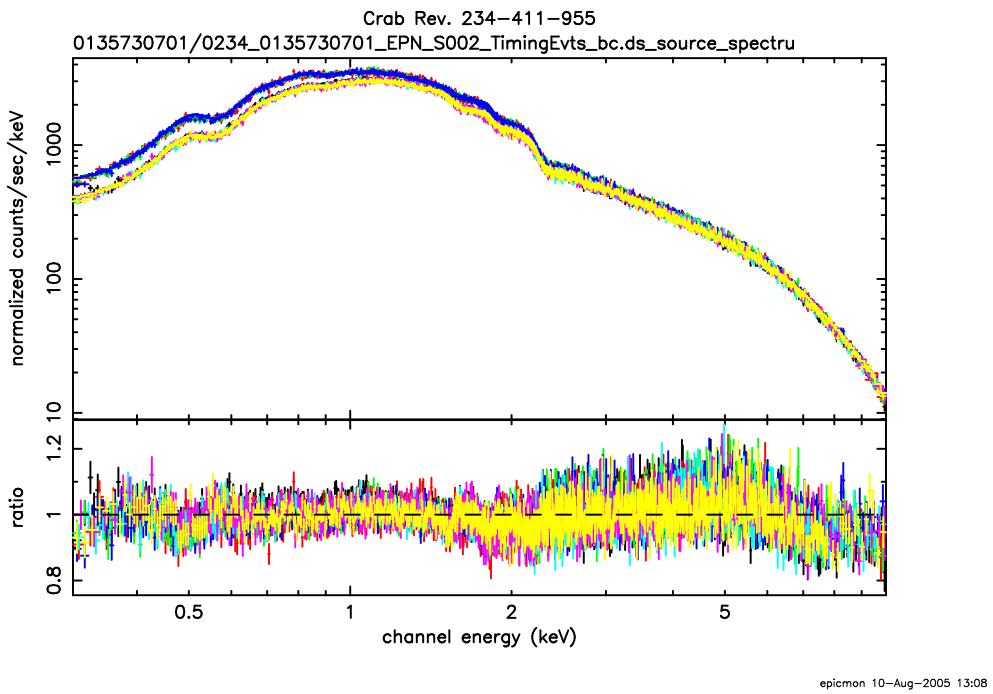

Figure 11: Spectra of the Crab in EPIC Burst mode

sis. We used the following setting to extract source and background regions: `((RAWX,RAWY) IN box(35.,71.5,20,70,0))`, and `((RAWX,RAWY) IN box(6,64,5,63.5,0))`, respectively. Spectra in the energy range 0.3–10 keV have than been extracted for Burst mode observations using single and double events only neglecting the events at CCD borders.
The spectra have been fit with a model constituted by photoelectric absorption (`wabs` implementation in XSPEC), and a power-law setting abundances to Wilms et al. (2000) and cross-sections as in Verner et al. (1997). Several residual features are known to be due to current uncertainties in the calibration. Fig. 11 shows the Crab (data and model) of the best fit to the EPIC-pn Burst mode spectrum. The best-fit parameters and results are summarized in Tab. 9. Note that the normalization of the Crab from that observations is not correct since the Crab is not fully imaged in the CCD. However extraction regions are now correctly treated by `arfgen` in Burst mode since SAS 6.1. This means that the normalization in Tab. 9 properly represent the flux of the section of the Crab Nebula, which falls onto the pn Burst Mode field-of-view.

Table 9: Crab best fit parameters.

Instrument	Γ	$Norm$ [photons $(keV)^{-1}$ cm^{-2} s^{-1}] @ 1 keV	N_H [10^{21}]	χ^2/ dof [keV]
p-n	$2.057\pm^{0.002}_{0.002}$	$7.13\pm^{0.01}_{0.01}$	$3.848\pm^{0.001}_{0.001}$	13635/10138

3.3 Relative timing of EPIC-pn

The EPIC-pn event analyzer (EPEA) uses the CDMU 1 Hz clock pulse to increment an internal 15 bit wide counter (FTCOARSE) and to reset a 16 bit sub-second (FTFINE) counter which is clocked with 48828.125 Hz. Thus the EPIC-pn CCD data frames are time stamped with a resolution of 20.48 ms by FTCOARSE/FTFINE pairs. In an ODF they form two columns in the first table of the EPIC-pn Auxiliary Data File (AUX) which are accessed by SAS in the process of converting frame counters to absolute photon arrival times.
In mid-2000 it was first discovered that the EPIC-pn AUX data exhibit certain kinds of anomalies whose frequency of occurrence is variable and apparently unrelated to camera mode, observing time or duration. This remains valid until today, i.e. some data sets are completely free of any problems others are heavily affected. Obviously all these problems need to be corrected for, as otherwise the event times turn out wrong. This is especially critical, as a single shift in FTCOARSE time will cause all subsequent times to be wrongly shifted by the same amount. Pulse profile analyzes with a data set that contains a single or multiple undetected and uncorrected such time jump will then be inconclusive because all photons after the instant of the time jump will be out-of-phase. This can result in a pulse peak broadening, phase shift or the appearance of spurious pulse components. Absolute timing analysis was likely impossible for obvious reasons. In the past these anomalies have all been seen and led to difficulties in the interpretation of obtained tentative results.
The SAS since the early days can reliably detect and correct for the anomalies. However, the detection logic seems to fail in some cases, with the consequences described above.
As of the SASv6.0 release we were in a state that all problems are reliably found and corrected for the fast EPIC-pn modes (Timing and Burst) however there might be still some rare cases of time jumps. This is still under investigation with a bulk reprocessing of all XMM-Newton data. Fig. 12 shows χ^2-epoch folding for different Crab observations, with a resolution of $\simeq 1 \times 10^{-10}$ s.
We performed χ^2-distributions of epoch folding for all Crab observations in the fast EPIC-pn modes. Each observation was folded using the radio period as a start value and the epoch of the respective radio period. We determined the X-ray period by calculating the weighted mean of the periods in each epoch folding using all periods for χ^2 values greater than 65 % of the maximum χ^2. We give the characteristic value for relative accuracy of timing analysis $\Delta P/P$ where $\Delta P = P_{radio} - P_{xray}$ and $P = P_{radio}$.
Fig. 13 shows the result of that analysis. The relative timing of XMM-Newton is considered better than some 10^{-8}.

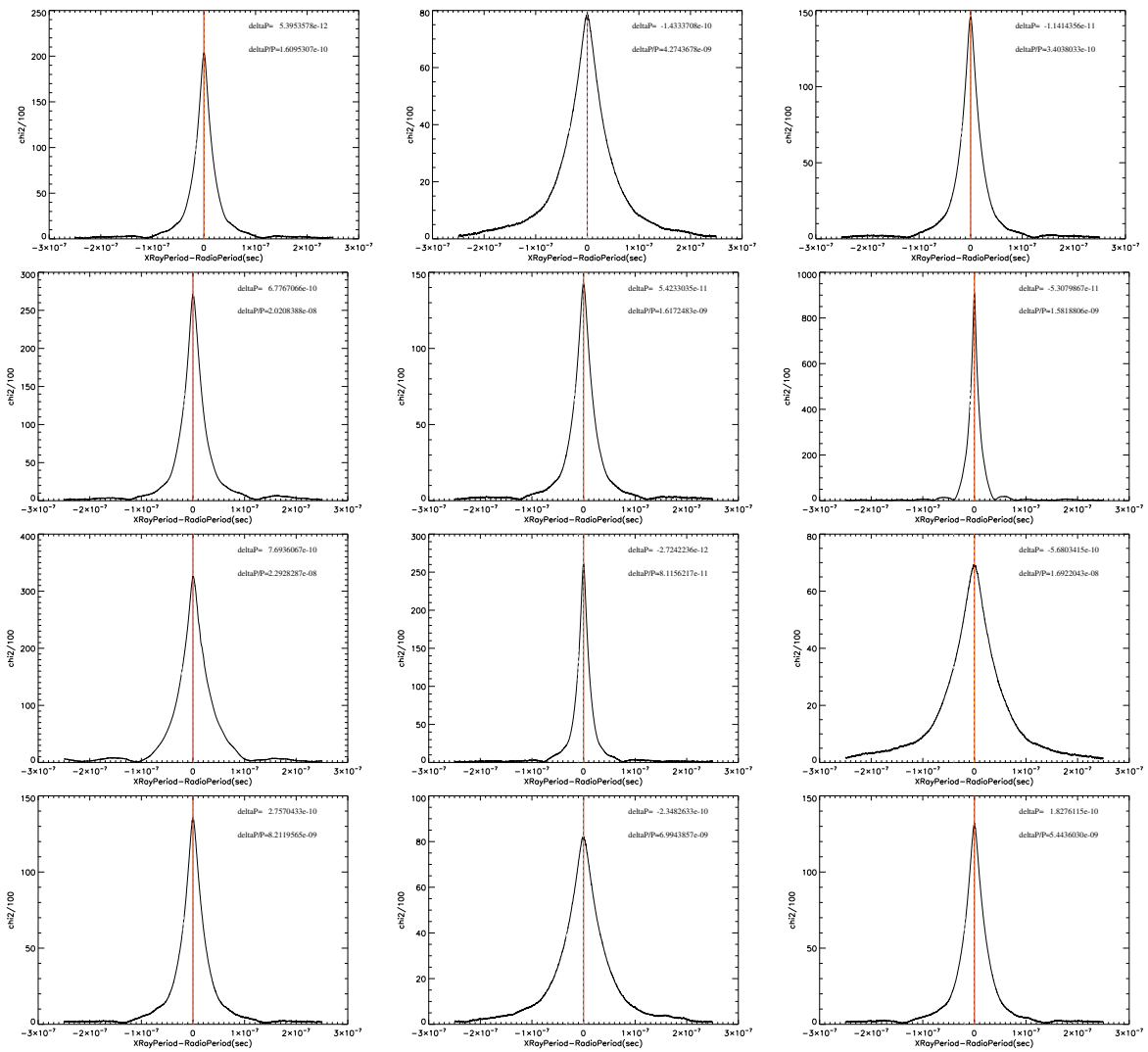

Figure 12: χ^2 epoch folding for different Crab observations. Note that all possible time jumps are corrected in the fast EPIC-pn modes and the χ^2 distributions is smooth as it should be.

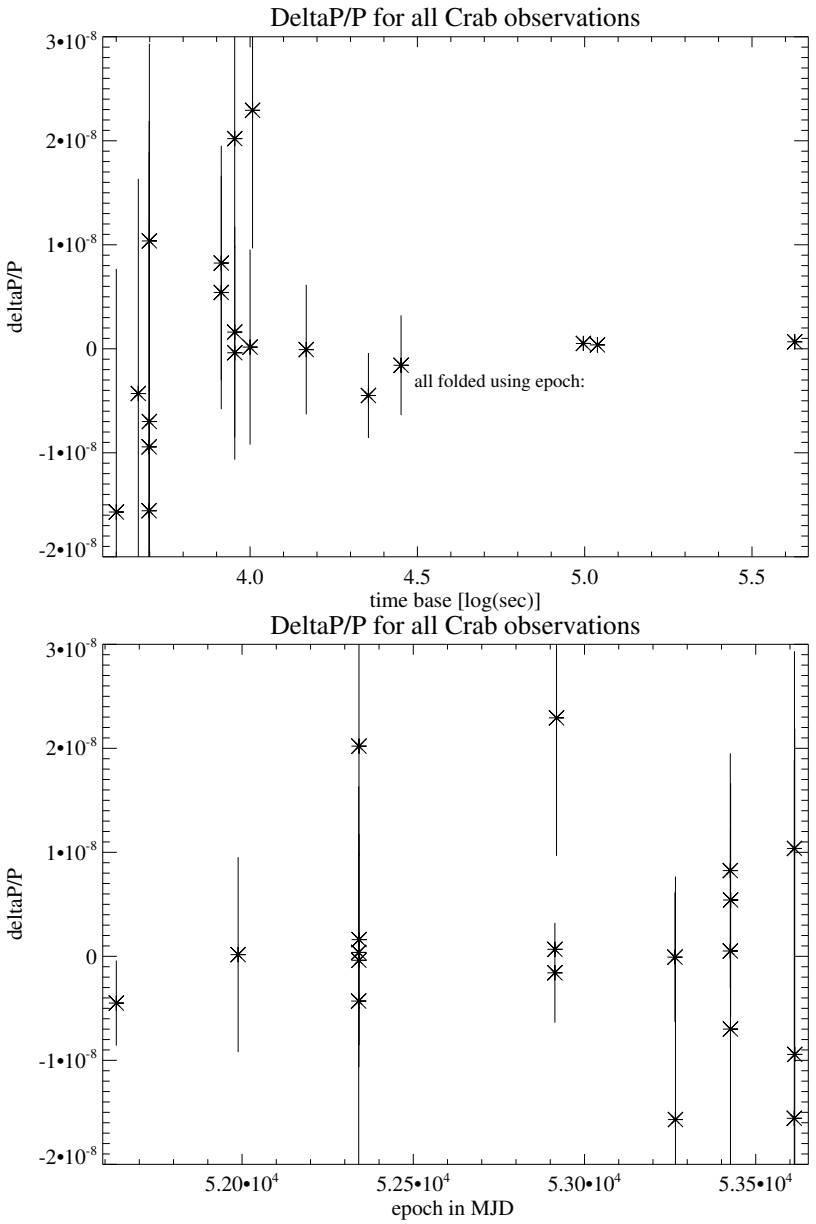

Figure 13: $\Delta P/P$ for all XMM-Newton Crab observations (EPIC-pn). *Upper panel*: the x-axis gives logarithmically the total time base of the observation (for longer observations the relative timing accuracy is obviously better.). *Lower panel*: the x-axis gives the epoch in MJD.

4 OM

4.1 SAS OM grism data processing

Processing of grism data was introduced by the first time with SAS version 6.0. Since then this functionality of the system has evolved considerably. The global scheme has not changed, but the implementation has been made more robust, and the results are clearer now.
The grism processing chain `omgchain` can be invoked with a new parameter, `extractfieldspectra` that allows the user to extract all spectra in the image (field spectroscopy) or at the contrary, to extract only the spectrum of the target sitting at the observation boresight (single object spectroscopy). The a priory knowledge of the position of the spectrum will be used by the chain task `omgrism` to look for the target spectrum among the results of `omdetect`.
If we consider that the majority of OM observations using grisms aim at single object spectroscopy, this capability makes the whole process faster and the results clearer. The output extracted spectra file (*SPECTR*) contains only the spectrum of the target (or a default extraction). The output list file (*SPECLI*) and the region file (*SPCREG*) allow the user to quickly verify the correctness of the extraction done.
In case of field spectroscopy, only the spectra that are uniquely identified (zero and first orders) are extracted.
Another improvement present in this SAS version 6.5 is the calibration of grism spectra. The previous calibration, in wavelength and absolute flux, was based in spectra extracted with IDL procedures. The algorithms used by SAS are different, mainly in the measurement of the background, and therefore the flux calibration was not entirely good. With SAS v6.5 we have released a new calibration based on spectral extraction performed by SAS. The whole system is now coherent.
The measurement of the position of the zero order, which defines the origin for the wavelength calibration, has been changed. Although in general the new method is more accurate, there are cases of very bright zero orders in the UV grism in which the measured position can be wrong by a few pixels. This converts into a shift of the wavelength scale. Future versions of SAS will correct this problem, which can be overcome now by extracting the spectrum interactively.
The interactive extraction of the spectra with `omgsource`, has been refined with respect to the previous version.
Finally, the standard pipeline run by the SSC at Leicester, based on SAS version 6.5 will include the processing of OM grism data.

4.1.1 Obs.#0125911301: HD 13499

HD 13499 is a F5V star. It has been observed several times as wavelength calibrator. In the field of view, there is also HD 13434 (F7V). This observation has been performed by off-setting the main target so as to have the spectra of both stars in a full frame low resolution exposure. Only the UV grism has been used, because both stars are too bright for the Visible grism.
`omgchain` has been run in field spectroscopy mode. The results of `omgrism` are depicted in Fig.14, where the changes, mentioned before, can be appreciated.
The measurement of the zero orders centroid is difficult because of their extreme brightness. For one of the stars (due to a close by straylight feature) there are several positions identified and the result is that the real spectrum is not properly extracted. The general background is very inhomogeneous due to the presence on straylight and this produces some spurious detections.
Note the default extraction performed at the boresight location, where there is no star because of the applied offset pointing.

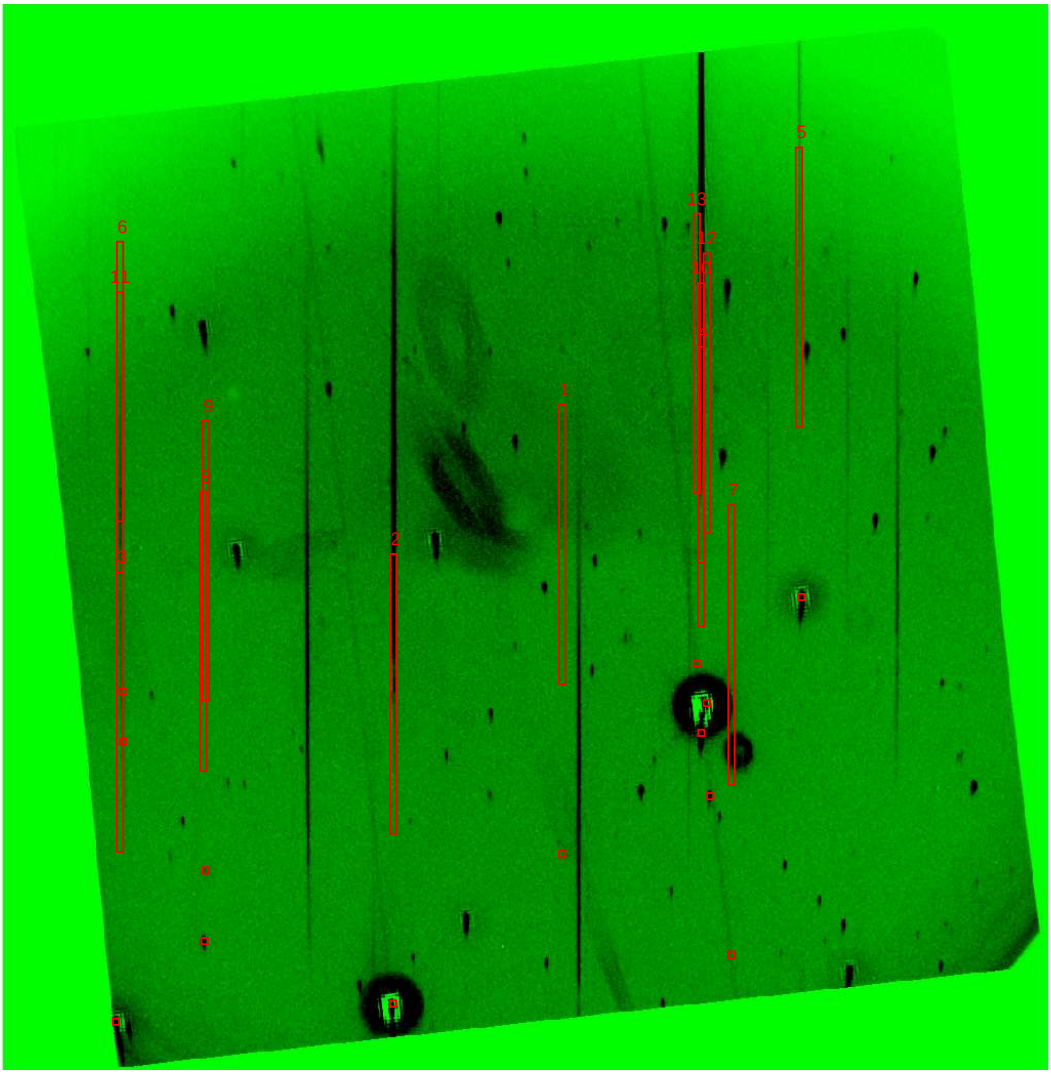

Figure 14: Detection of spectra obtained with the OM UV grism in the field of HD 13499 (the bright object on the mid-right part of the image)

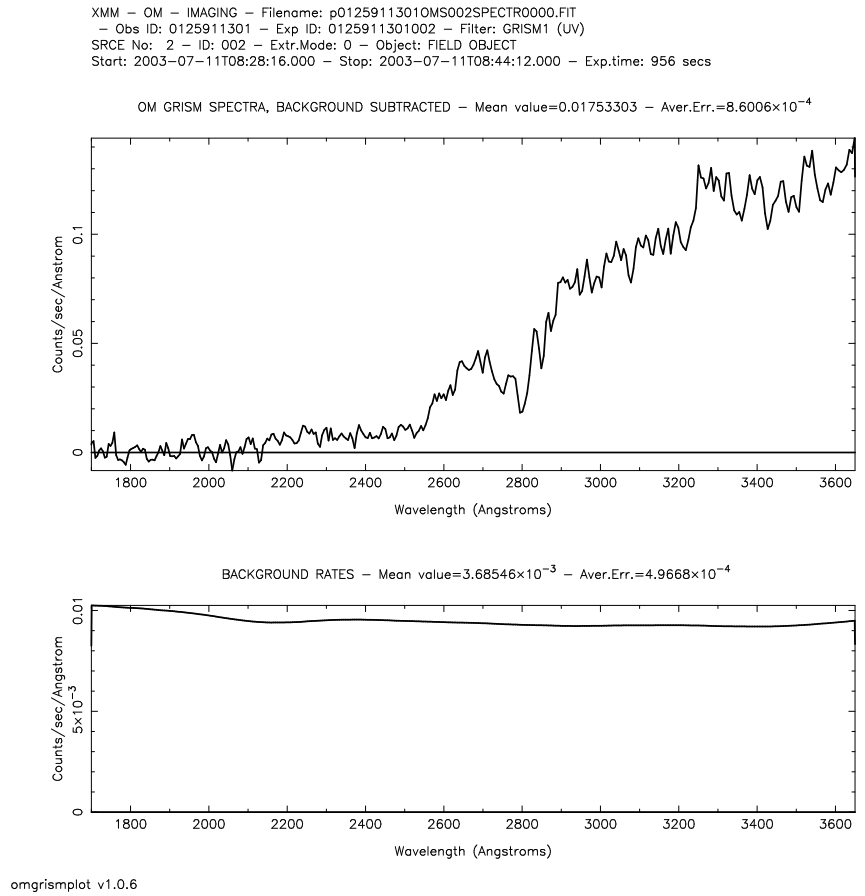

Figure 15: Extracted UV spectrum of HD 13434. Note the Mg II absorption feature at 2800 Å

`omgrism` is able to extract correctly the spectrum of one of the two stars. Figure 15 shows the extracted net spectra and background in count-rate versus wavelength. The solution for the other bright star is to use the interactive task `omgsource` (see below).

4.1.2 Obs.#0125910901: HZ 2

HZ 2 is a white dwarf standard star. It is one of the standard stars used to derive the flux calibration of the grisms. It has been observed several times. This ODF is used to check the consistency of the whole SAS processing of OM grism.
The observation was performed in User Defined mode. Fig. 16 shows the extraction regions determined by `omgrism` in the Visible and UV grism images, after running `omgchain` in single object mode (the default). The target spectra are detected in both grisms. Other zero and first orders are ignored. The flux calibrated spectra of HZ 2 are presented in Fig. 17 and 18. The Visible spectrum shows clearly some hydrogen lines. The small scale, noise-like ripple features in both spectra are due to the "Modulo 8" pattern present in the image, which cannot be entirely corrected by `ommodmap`.

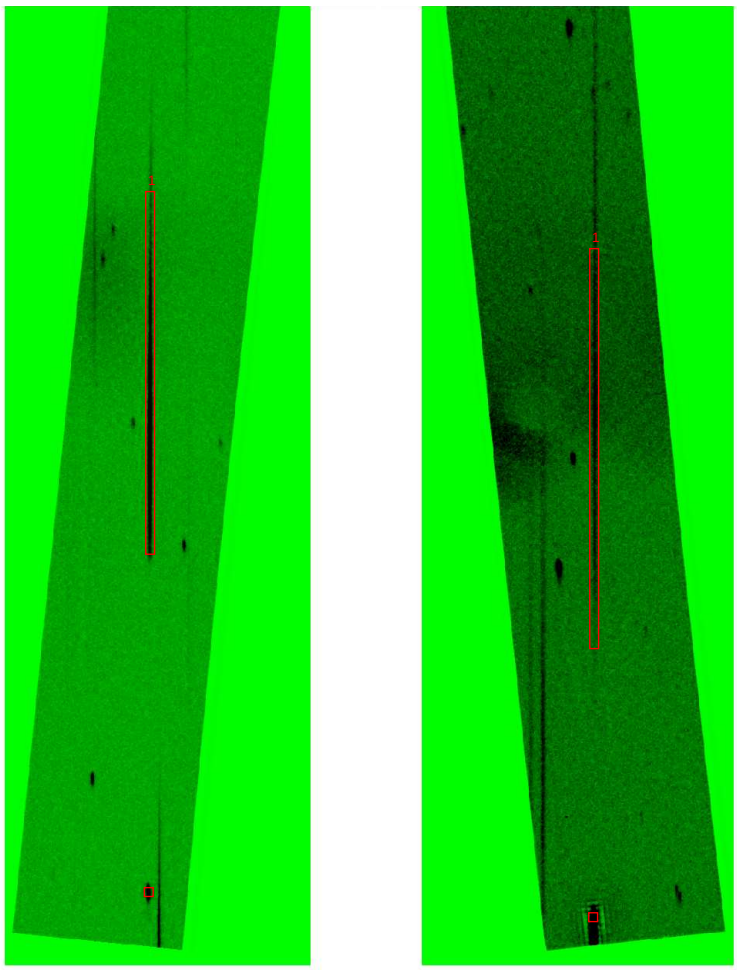

Figure 16: Extraction region of spectra in HZ 2. *Left*: visible grism. *Right*: UV grism

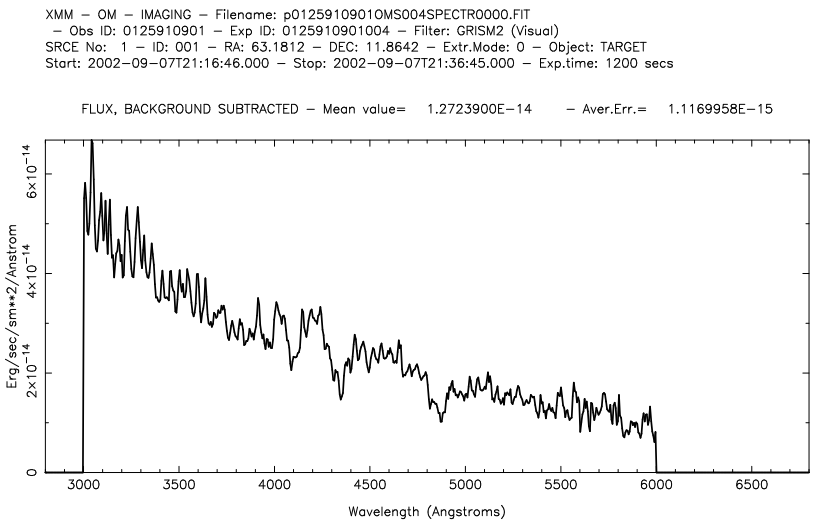

Figure 17: Flux calibrated Visible grism spectrum of HZ 2. Hydrogen β, γ and δ lines are clearly visible

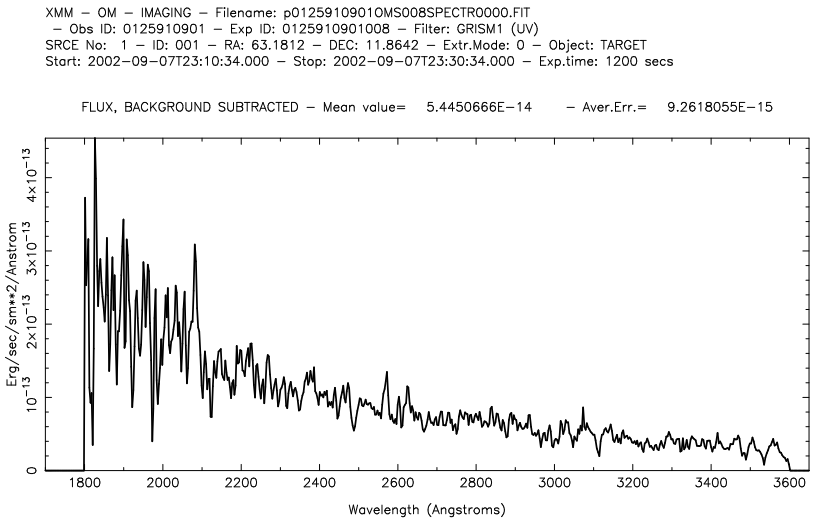

Figure 18: Flux calibrated UV grism spectrum of HZ 2

4.2 SAS interactive tasks validation

4.2.1 `omsource`

`omsource` is an interactive SAS task to perform aperture photometry on OM images. This task works on SAS processed images (after flat-field and "Modulo 8" corrections). The user can modify the default parameters for source and background count rates estimation. A source list obtained with `omdetect` can be loaded on the image to modify the photometry of previously detected sources or to add new ones.
After selecting the source (previously detected or not) with the cursor, the task performs all necessary corrections, producing a new source list or modifying an existing one.
We have tested `omsource` using several exposures of the BPM16271 observation with various filters. The task works well, and the results are compatible with the ones obtained automatically by using `omichain`.

4.2.2 `omgsource`

The interactive grism extraction task `omgsource` has been used in the data of HD 13499. We can see in Fig. 19 the interface layout showing different control parameters and examples of spectra selection.
The spectrum whose extraction failed when running automatically `omgchain` has been extracted. The interactively extracted spectrum of HD 13499 (see Fig. 19) is presented in Fig. 20. Since the zero order centroiding is determined by the selection done with the cursor and not by the fake detections provided by `omdetect` in the field spectroscopy mode, the wavelength scale is correct.

4.3 Calibration items

4.3.1 OM filter photometry

SAS v6.5 includes by the first time a correction for time sensitivity degradation. This effect, which amounts up to 2.8% per year in the UV filters and less than 2% in the optical ones, could only be measured after a few years of OM operations and it is now corrected by the SAS

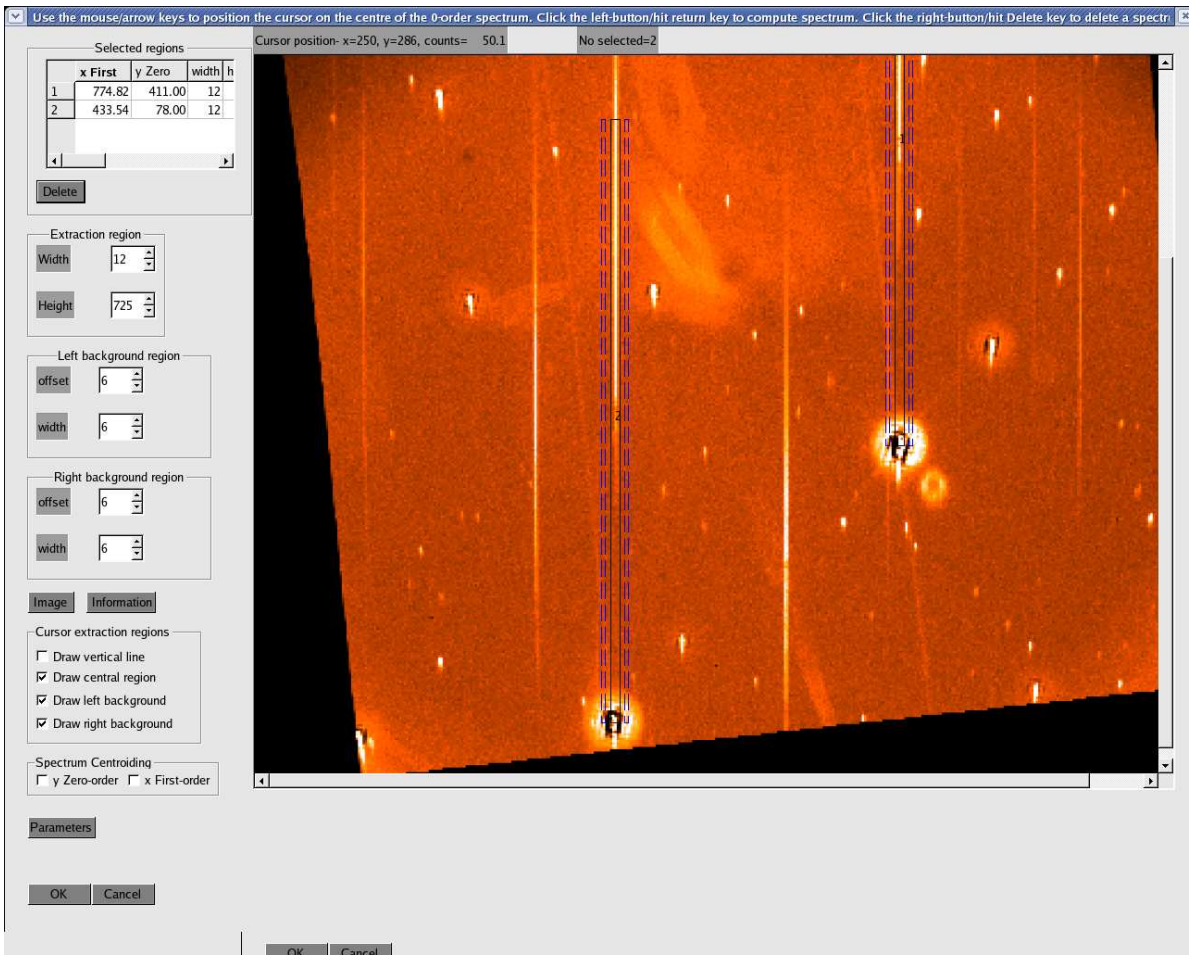

Figure 19: Interactive extraction of UV grism spectra in the field of HD 13499

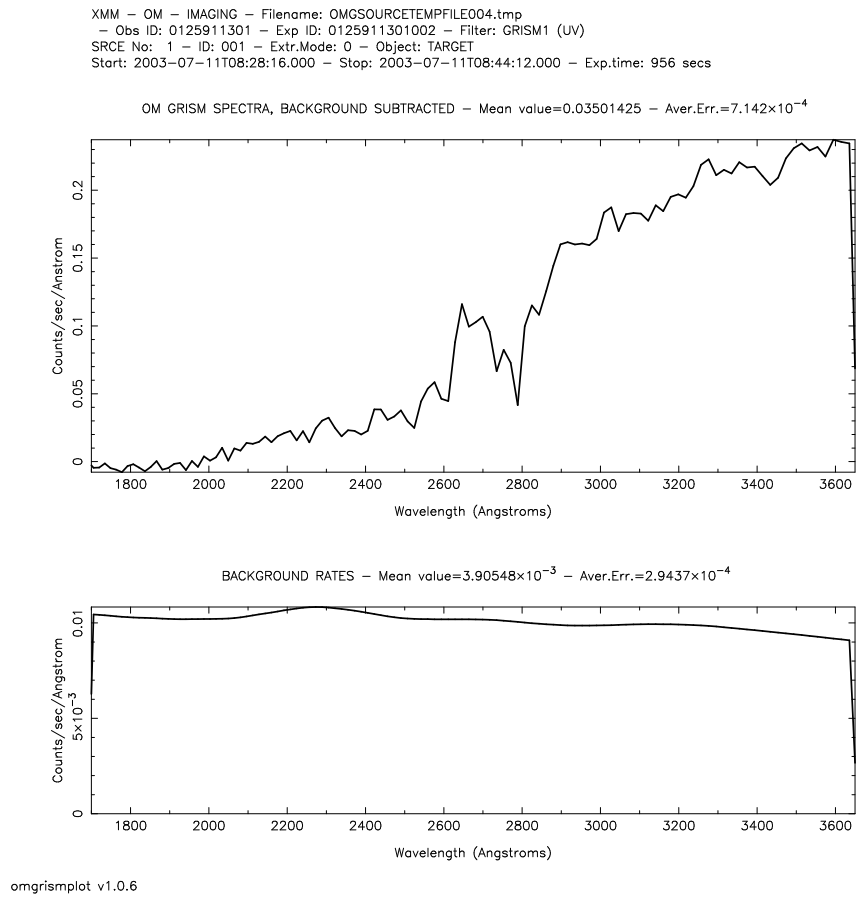

Figure 20: Interactively extracted UV grism spectrum of HD 13499. The Mg II absorption feature at 2800 Å characteristic of F-type stars, is clearly seen.

Table 10: The Standard Johnson UBV magnitudes of the BPM 16274 from Eggen and XMM-Newton OM.

	U	B	V
Eggen's values	13.375	14.185	14.20
derived from OM	13.339	14.194	14.205

Table 11: The OM count rates and flux densities of BPM16274

	V	B	U	UVW1	UVM2	UVW2
OM count rates	31.90	106.75	112.11	70.58	28.37	14.14
conversion factors	2.49E-16	1.29E-16	1.94E-16	4.76E-16	2.20E-15	5.71E-15
Flux densities	7.94e-15	1.38e-14	2.17e-14	3.36e-14	6.24e-14	8.07e-14

OM image processing. The count rates measured in the detected sources are now corrected and referred to a zero epoch, defined around Rev.#324.
The white dwarf BPM 16274 is an OM routine calibration target, which is used for monitoring OM performance and calibration. The observation used in this report took place on May 13, 2001, Rev.#261. It contains exposures with all filters. Time sensitivity degradation is negligible in this observation since it is very close to the zero epoch defined for this effect.
The standard Johnson U, B, V magnitudes of the BPM 16274, reported by Eggen, are compared with the magnitudes obtained with OM (see Tab. 10). SAS converts the measured instrumental magnitudes u,b,and v (13.134, 14.194 and 14.204 respectively) into standard UBV by using the transformations given in the OM_COLORTRANS CCF.
In order to convert the OM count rates to flux, the flux conversion factors derived from the observations of several white dwarfs standard stars can be used. These factors are also given in the OM_COLORTRANS CCF. The results are presented in Tab. 11, where we give for each filter the count rates (counts/s) and the corresponding flux densities (erg/cm^2/s/A).
In Figure 21 we can see the fluxes obtained with the OM UV filters superimposed on a spectrum of BPM 16274 obtained with IUE.

4.3.2 OM astrometry

OM astrometry has been verified using the observation of BPM 16274. Not only the target itself, but all stars in the field of view have been considered for this validation.
Two tasks in `omichain` allow us to perform a cross correlation of the computed positions with a catalogue file. These are `omatt` and `omsrclistcomb`. If the correlation is successful, the computed offsets are written in to the source list, and two columns with corrected coordinates are added to the list as well. `omatt` works on an individual exposure with any filter, and `omsrclistcomb` takes the final combined (for all used filters) source list to compute the overall offset with all available information from the observation.
In Fig. 22 we present the results for the observation of BPM16274 with the V filter. Similar results are obtained in all filters.
The final source list contains 480 sources and 40% of them were matched with a subset of the USNO catalogue. The final offsets computed by `omsrclistcomb` are -3.7 arcsec in right ascension

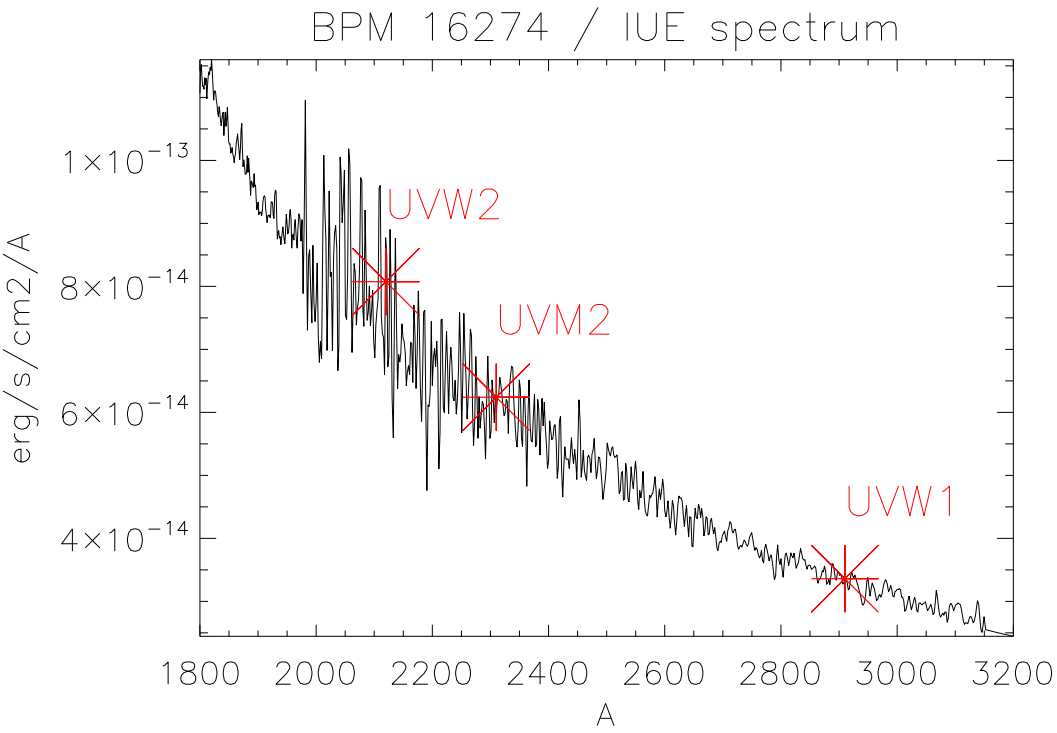

Figure 21: Fluxes obtained with OM UV filters in BPM 16274 compared with an IUE spectrum of the star.

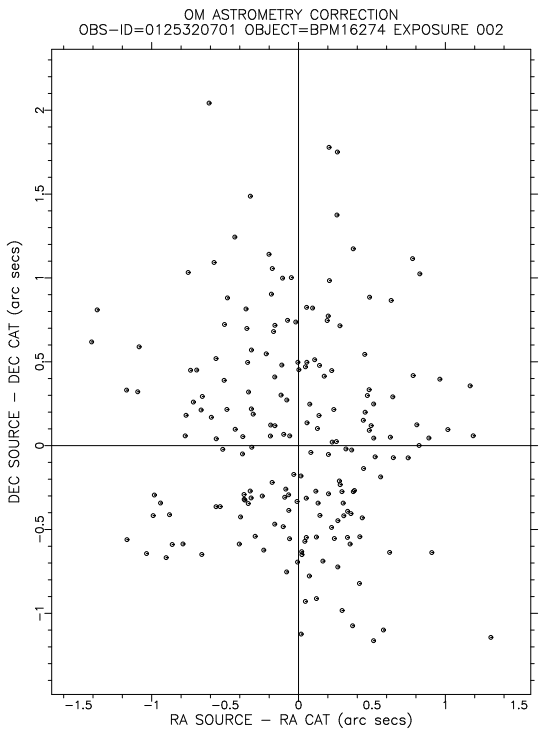

Figure 22: Astrometry in BPM 16274 field. Offsets in V filter

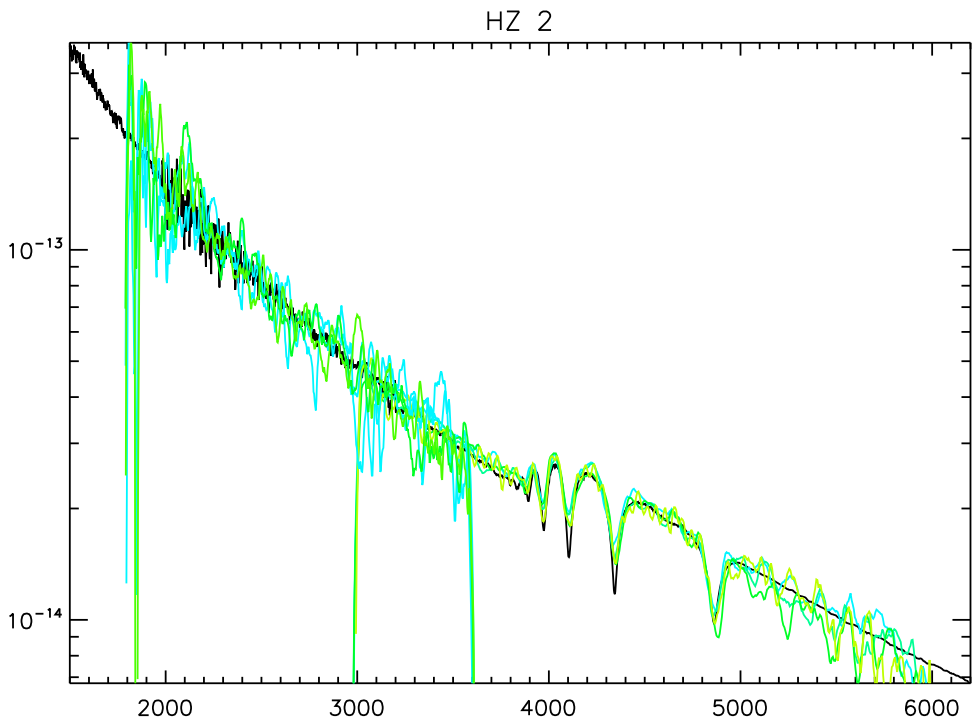

Figure 23: Flux calibrated spectrum of HZ 2. Standard flux is given in black. In blue and green we depict several spectra obtained with the OM UV and Visible grisms.

and 1.31 arcsec in declination. The RMS residual of the correlation after correction is 0.8 arcsec. If we look at the source itself, we find after correction an offset from the catalogue coordinates of -0.9 and 0.2 arcsec in right ascension and declination respectively. Individual star offsets vary with the distance to the center of the field of view. This is due to inaccuracies in the distortion correction applied to the data.

4.3.3 OM grisms wavelength scale and flux calibration

The main source of error in the grism wavelength scale is due to the determination of the centroid of the zero order. The analysis of the data of this Science Validation and also of other grism data, performed by the OM Team at ESAC, shows that discrepancies of a few, 3 or 4, pixels produce shifts in the wavelength scale of up to 10 Å for the UV grism and 20 Å for the Visible one. As we mentioned before, there may be cases as the one presented in Fig. 14, where the detection of the zero order is perturbed by its excessive brightness or by other close-by spectra or image features. This can produce displacements on the scale of more than 50 Å. These cases are handled much better by using the interactive task `omgsource` which allows the user to constrain the centroiding as shown in Figs. 19 and 20.
The accuracy of the wavelength scale can be appreciated in Fig. 23, where the hydrogen lines of HZ 2 in the OM Visible grism spectrum of the star appear superimposed on its standard spectrum obtained from the HST `Calspec` database.
The grisms flux calibration is based on observations of several standard stars, one of which is HZ 2. We have performed a consistency check by comparing the flux given by SAS processing for this star with its original standard flux. Fig. 23 presents such a comparison. All spectra

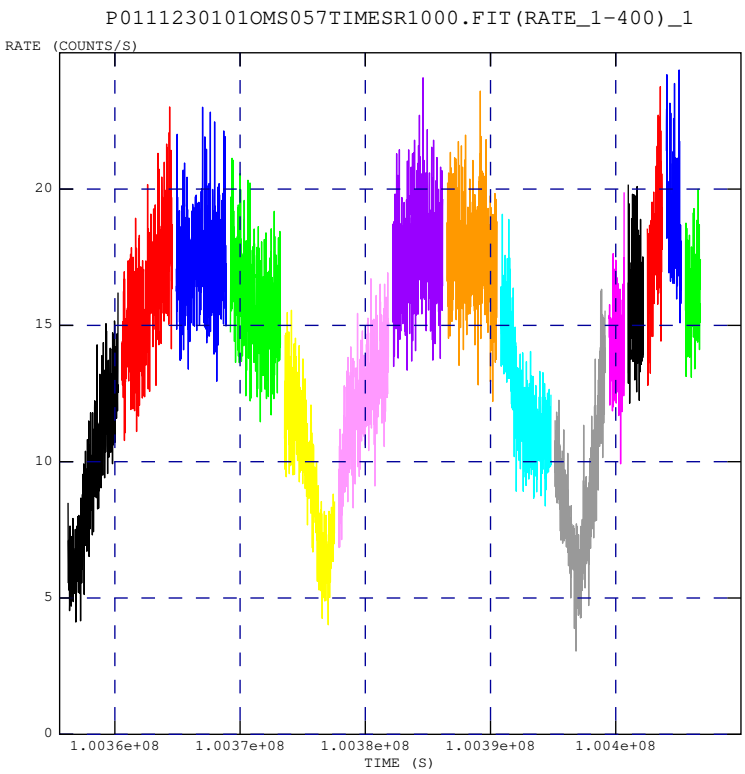

Figure 24: The OM UVW1 light curve of the low-mass X-ray binary X1822-371.

of this star obtained with OM grisms are over-plotted on top of its standard spectrum. The average differences are less than 5 % in both grisms. (Errors are larger at the short wavelength end of the UV grism and at the long wavelength end of the V one).
The excellent agreement of both grisms in their common wavelength region, between 3000 Å and 3600 Å can be appreciated in this figure too.

4.3.4 OM Fast Mode timing accuracy

X1822-371 is a low-mass X-ray binary which was observed with XMM-Newton on March 7, 2001, Rev.#228. The observation was performed with OM in FAST mode using the UVW1 filter.
A total of 15 exposures were obtained (OM image & fast default mode).
Processing with SAS `omfchain` produces one light curve per exposure. We show all of them in Fig. 24. (It should be noted that SAS does not contain a task to concatenate these light curves.) This figure shows almost 2.5 cycles of the star. The last five exposures were shorter than the first ones.
The period derived from the OM light curve is about 5.67 hours, in good agreement with the one obtained from the EPIC-pn light curve.
The output of `omfchain` contains also an additional set of time series and light curves. This occurs because of the presence of a star close to X1822-371, which enters partially in the fast mode window. This star is detected in some of the exposures, as it is shown in Fig. 25. Whenever this happens, additional light curves are produced.

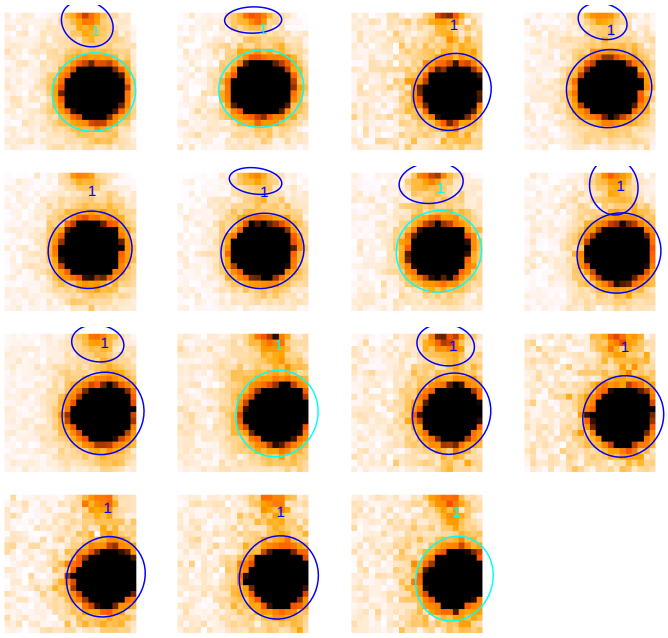

Figure 25: OM fast mode windows showing the presence of another star close to the low-mass X-ray binary X1822-371. Its light curve is also extracted.

5 RGS

5.1 Small but significant revision to the default behavior of `rgsproc`

The RGS SAS meta-task `rgsproc` is the tool almost invariably used for the production of high-resolution RGS spectra and their associated response matrices. With each release of the SAS, including SAS v6.5, a test harness is run on a set of observations for validation purposes. With this release, the default treatment of the background has been changed so that source spectra are not background corrected. Thus so-called "TOTAL" spectra are produced containing contributions from both source and background as opposed to "NET" spectra, in which an estimate of the background has already been subtracted. This has two main advantages: first, it allows a more rigorous statistical treatment given that the Poissonian character of the data is preserved, with the absence of any apparently negative fluxes; and second, it is straightforward to be able to use alternative background estimates to the off-axis `BGSPEC` produced automatically by `rgsproc`, such as, in particular, the independent `MBSPEC` background estimates calculated by the task `rgsbkgmodel`. Of course, these advantages require explicit use of a background spectrum in XSPEC, for example. Estimates of physical parameters are expected to change insignificantly. The meta-task `rgsproc` was run on the Obs.#0099280201 observation of Mkn421 (Rev.#195) with defaults settings including those concerning data selection. No account was taken of a few short periods of slightly higher background. Results from the simultaneous XSPEC analysis of the resulting set of four total and background spectra, from RGS1 and RGS2 first and second order, are shown in Fig. 26. In this example, a simultaneous fit to the 4 spectra using a broken power-law model in the recommended RGS wavelength range of $6 \leq \lambda(\text{Å}) \leq 38$ gave the parameter estimates reported in Table 12. The likelihood C-statistic is the proper choice for the analysis of RGS (and all other) data.

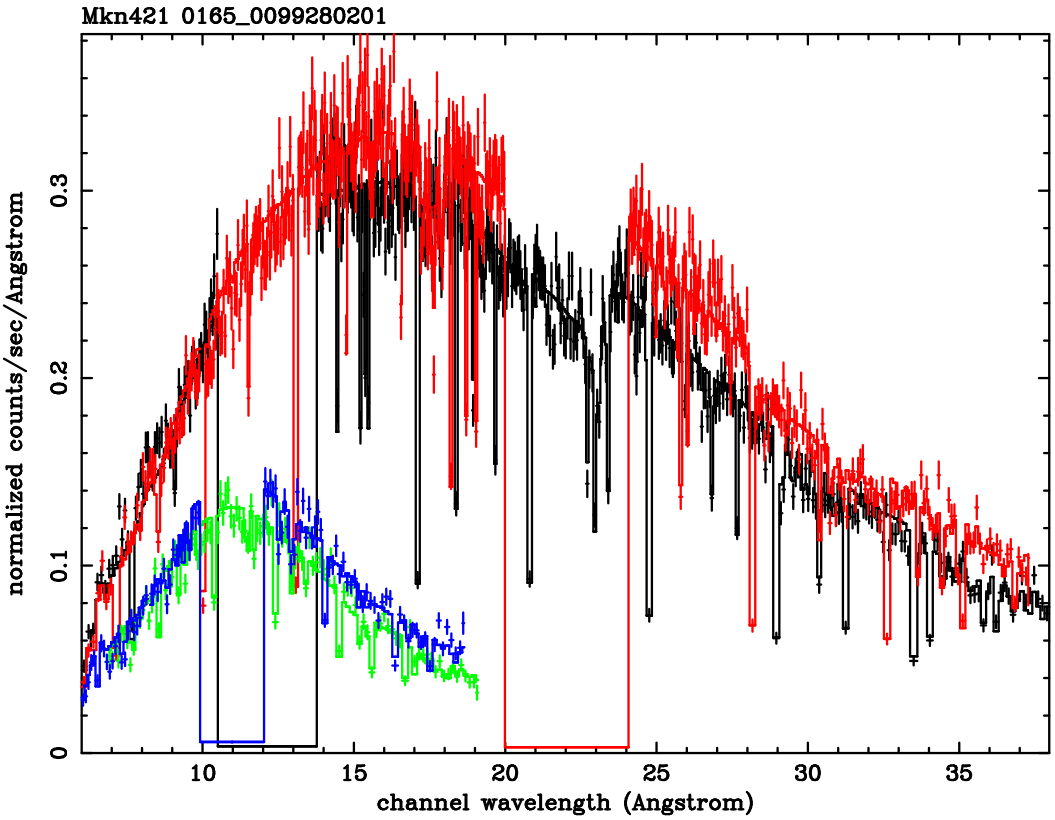

Figure 26: Mkn421 spectra from RGS1 1st order (black); RGS2 1st order (red); RGS1 2nd order (green); and RGS2 2nd order (blue); fitted with an absorbed broken power-law model. Prominent low-counts spectral bins are due to gaps between adjacent chips.

TBabs	N_H	$8.78\pm1.10\times10^{19}$	cm^{-2}
bknpower	Γ_1	2.18 ± 0.02	
bknpower	E_{break}	0.73 ± 0.01	keV
bknpower	Γ_2	2.42 ± 0.01	
bknpower	Normalization	$7.84\pm0.02\times10^{-2}$	RGS1 order 1
bknpower	Normalization	$7.56\pm0.02\times10^{-2}$	RGS2 order 1
bknpower	Normalization	$7.66\pm0.04\times10^{-2}$	RGS1 order 2
bknpower	Normalization	$7.19\pm0.04\times10^{-2}$	RGS2 order 2
C-statistic = 10294.36 using 8744 PHA bins			

Table 12: Mkn 421 parameters of the best-fit broken power law model of first and second order spectra of RGS1 and RGS2. The 1σ statistical errors were calculated with the `XSPEC> error` command. The discrepancies between between the different normalizations exceed these statistical errors and arise from residual systematic calibration errors at the few percent level.

5.2 The use of `rgsfluxer`

The new default absence of background subtraction from source spectra by `rgsproc`described above in section 5.1 put a new requirement on the task `rgsfluxer` to take explicit account of the background when calculating its wavelength-dependent qualitative estimates of source flux. This is especially important for weaker sources and was achieved through an additional parameter named `bkg`. Fig. 27 shows the 1st-order fluxed spectra from four observations of AB Dor using the simultaneous off-source `BGSPEC` background estimates calculated by `rgsproc`. The RGS background rises quite sharply above the instrumental silicon edge at 6.74Å, so the good behavior of the fluxed spectra at the shortest wavelengths confirms that a proper background correction has been made.
The new `rgsfluxer` works correctly with the default `BGSPEC` files for which it was designed but does not handle correctly the independent background estimates produced by `rgsbkgmodel`.

5.3 The RGS wavelength scale

The assertion made above in section 5.1 that the more rigorous statistical treatment of data enabled by the explicit use of background models should have little affect on parameter estimates of the strengths and positions of spectral lines has been assessed by comparing the latest XSPEC models of a line-rich coronal spectrum of AB Dor with those calculated during the previous SAS validation exercise. Table 13 shows the differences in the best-fit line positions and fluxes between SASv6.5.0 and SASv6.0.3. The strongest lines in the spectrum show differential line shifts of a milliÅ or less and strengths within 2% of the earlier estimates. As expected, the weakest lines are those most affected by the change of background method. In the worst case, for the weak N VI triplet - almost invisible in Fig. 27 unless you know where to look - the apparent flux increased by 7% and the wavelength moved 16mÅ to the red. Similarly, the weak Si XIII triplet is in the short-wavelength region where the RGS effective area is decreasing rapidly and where the background is high. It suffered comparable apparent changes.

5.4 New RGS tasks in SAS v6.5

5.4.1 `rgscombine`

The task `rgsproc` enables the user to calculate time-resolved RGS spectra for any interval upto the length of an individual exposure. This limitation has been overcome with the release of

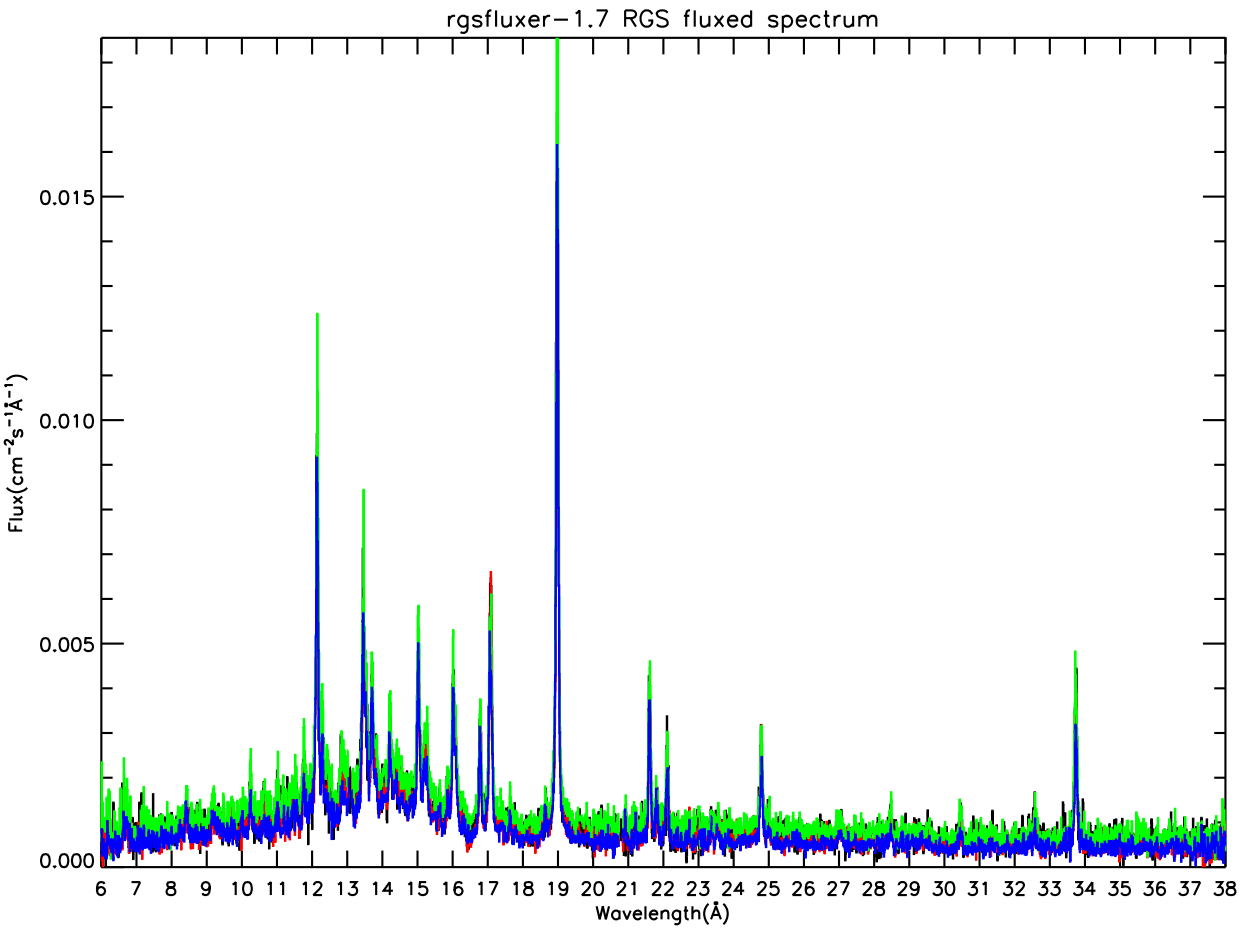

Figure 27: AB Dor 1st-order fluxed spectra produced by `rgsproc` for the 4 observations 0185_0133120201 (black); 0338_0134521301 (red); 0462_0134521601 (green); and 0572_0134522201 (blue). The black, red and blue spectra were of almost equal intensity.

ion	$\lambda_{\rm lab}$ (Å)	$f_{\rm SASv6.5}$ (10^{-5} cm^{-2} s^{-1})	$\Delta\lambda_{\rm SASv6.5}$ (mÅ)	$(\Delta f/f)_{\rm SASv6.5}$ (%)
C VI	33.7396	13.1	−0.2	−6.7
N VI	28.7871	2.5	+15.9	+7.1
N VII	24.7793	16.0	−1.0	+2.3
O VII	21.6020	35.1	+1.2	+1.4
O VIII	18.9671	125.9	+0.1	+1.4
Fe XVII	15.0150	48.4	+0.6	+2.7
Ne IX	13.4471	56.2	−1.6	+0.7
Ne X	12.1321	65.8	+0.0	+0.8
Mg XI	9.1688	5.2	−4.1	−8.8
Mg XII	8.4192	4.4	−2.9	−2.0
Si XIII	6.6480	5.0	+7.7	−14.8

Table 13: Changes between SASv.6.0.3 and SASv.6.5.0 in the best-fit δ-function line-model parameters for the principal ions in the Obs.#0133120201 RGS1 spectrum of AB Dor.

the task `rgscombine` which allows the combination of any number of individual component spectra into a single combined spectrum with the appropriate combined response matrix and background spectrum to enable quantitative analysis. The combined spectrum has the expected overall exposure time and count rate as shown in Table 14. The increased statistical weight of

rev	Obs#	RGS1 spectrum	time (s)	rate (s^{-1})	RGS2 spectrum	time (s)	rate (s^{-1})
0185	0133120201	R1S001SRSPEC1003	20490	1.088	R2S002SRSPEC1003	19756	1.341
0338	0134521301	R1S001SRSPEC1003	38616	0.941	R2S002SRSPEC1003	37532	1.210
0462	0134521601	R1S001SRSPEC1003	42835	1.271	R2S002SRSPEC1003	41687	1.552
0572	0134522201	R1S001SRSPEC1003	50863	0.872	R2S002SRSPEC1003	50854	1.145
		Σ	152804	1.030	Σ	149829	1.300
		`rgscombine`	152804	1.030	`rgscombine`	149829	1.300

Table 14: Comparison of exposure times and count rates from component and combined RGS1 and RGS2 1st-order spectra. The net source count rate is as reported by the command `XSPEC> show rates`.

the combined data allows, for example, a more sensitive search for weak lines as illustrated in Fig. 28.

5.4.2 `rgssuperrmf`

This task was designed to complement `rgscombine` to enable direct calculation of a combined spectrum, background and response matrix without the need, in particular, for a set of individual response matrices. For high-resolution work, this would save considerable disk space. Unfortunately the task fails.

6 Conclusions

The main conclusion of the EPIC SASv6.5 SV exercise can be summarized as follows:

- SAS v6.5 can reduce data taken with all the EPIC, OM, and RGS scientific modes

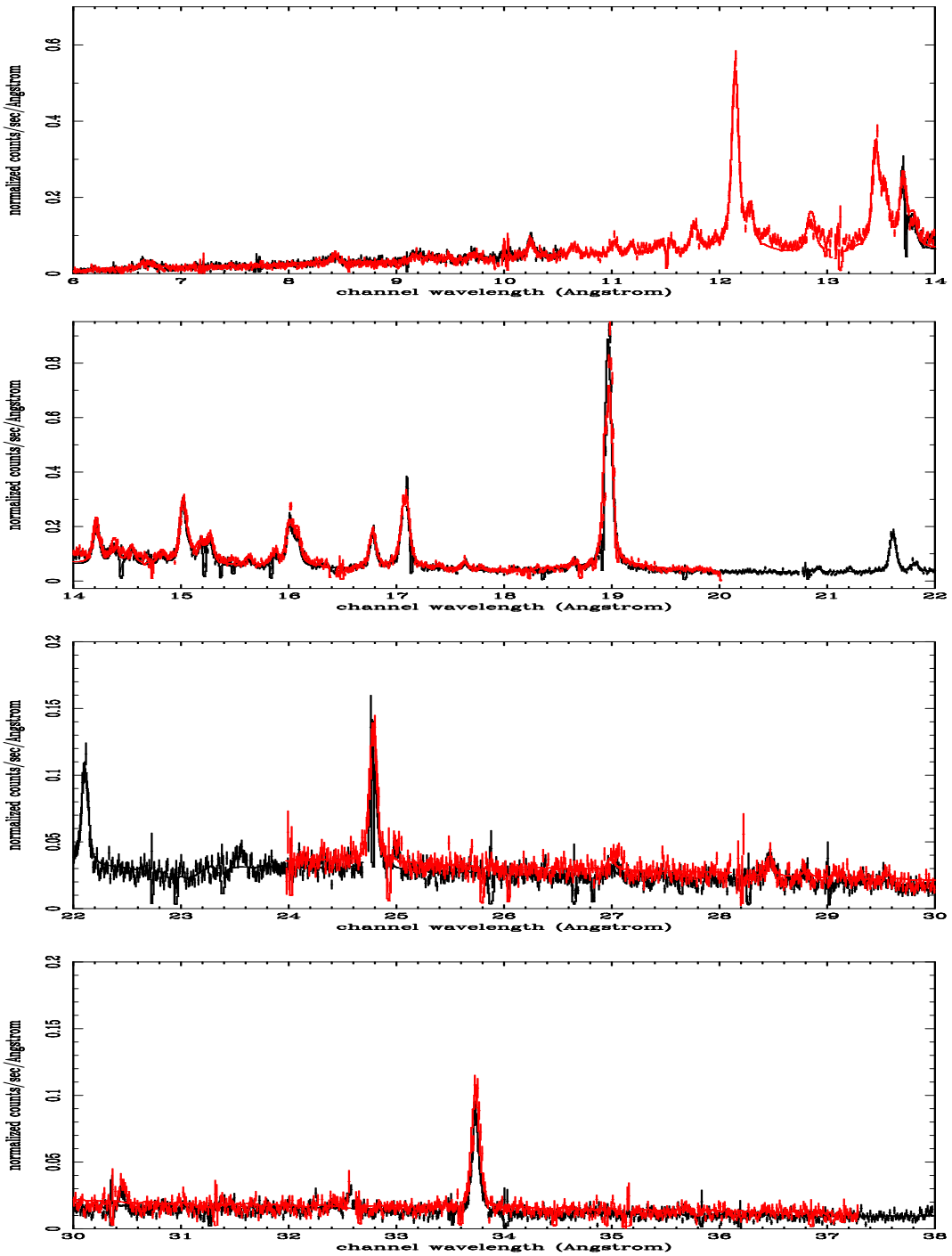

Figure 28: XSPEC plot of analysis following the application of `rgscombine` to 4 spectra of AB Dor. RGS1 is shown in black and RGS2 in red. A model made up of continuum and 84 delta-function lines has been fit simultaneously to the combined 1st-order spectra of RGS1 and RGS2 using the combined background spectra and response matrices also produced by `rgscombine`. The 4 different wavelength sections have different vertical scales. Data points have error bars while the solid lines show the best-fit model.

- event list produced with the `chain`s and the `proc`s, albeit not identical, yield scientifically indistinguishable results
- the quality of EPIC spectral fitting is significantly improved with SAS v6.5. Residuals are within ±5% for all Imaging and Timing Modes across the whole sensitive bandpass
- the relative timing accuracy of the pn camera is $\lesssim 3 \times 10^{-8}$
- the flux cross-calibration among the EPIC cameras is better then 5%, once again improving with respect to previous SAS SV excercises
- SAS v6.5 corrects well for the low sensitivity patch recently discovered close to the MOS camera boresight, as well as for any associated MOS1 bright columns, *as long as* the latter features are not too close (1–2 pixels) to the centroid of the PSF
- SAS v6.5 improves significantly the scientific accuracy of the analysis of grism OM exposures. If the identification of the zero order is correct, typical photometric accuracies of ≃5% can be achieved. Uncorrect determination of the 0th order centroid can introduce systematic shifts in the wavelength reconstruction as large as 50Å. In these cases, analysis with the new interactive task `omgrism` is recommended, and reproduce the expected calibration accuracies
- SAS v6.5 includes for the first time a correction for OM time-dependent sensitivity degradation
- the SAS v6.5 version of `rgsproc` produces by default total (*i.e.*, not background-subtracted) spectra, allowing more flexibility in the data analysis. `rgsfluxer` has been as well adapted to work with total spectra.
- a new task is available (`rgscombine`), which allows users to combine an arbitrary number of individual component spectra with the appropriate combined response matrix and background spectrum

References

Kirsch M.G.F., et al., 2005, SPIE, in press (astro-ph/0508235)
O'Brien P.T., et al., 2001, A&A, 365, L122
Verner D.A., et al., 1996, ApJ, 465, 487
Warwick R.S., et al., 2001, A&A, 365, 248

Appendix A: Matrix of supported instrument modes by SAS v6.0

In Tab. 15 we show the list of science instrument modes which can be processed by the SAS, and are currently being routinely processed by the pipeline.

Appendix B: *Can*s and *Can't*s for SAS v6.0

This page provides a quick summary of what can and what can't be done with the SAS version discussed in this document. Moreover, it summarizes the status of the PPS data product processing.

Table 15: XMM-Newton instrument scientific modes supported by the SAS and the PPS

Mode	Processed by SAS?	Processed by PPS?
	MOS	
Full Frame	Y	Y
Large Window	Y	Y
Small Window	Y	Y
Timing Uncompressed	Y	Y
	pn	
Full Frame	Y	Y
Large Window	Y	Y
Small Window	Y	Y
Fast Timing	Y	Y
Fast Burst	Y	Y
Extended Full Frame	Y	Y
	RGS	
Spectroscopy	Y	Y
	OM	
Image Mode	Y	Y
Fast Mode	Y	Y
Full Frame Low Resolution	Y	Y
Full Frame High Resolution	Y	Y
Science User Defined	Y	

- What SAS can do now (in brackets the SAS module responsible for the task)
  - run tasks either from the command line or through the interactive GUI
  - create script and session logs
  - create Calibration Index Files tailored to the user analysis conditions (`cifbuild`)
  - apply barycentric corrections (barycen)
  - With EPIC data
    - generate calibrated event lists (`e[mp]proc`, `e[mp]chain`)
    - extract scientific products (light curves, spectra, images) for all instrumental modes (`evselect`, `xmmselect`) from event lists. Event lists can be filtered by the user (`selectlib`).
    - run source detection algorithms on images (`edetect_chain`)
    - create Good Time Intervals from time-varying data (`tabgtigen`) and apply them to the scientific product extraction
    - create response matrices (*arfgen*; `rmfgen`) for all modes, both for point-like and extended sources
  - With RGS data
    - generate calibrated event lists (`rgsproc`)
    - run the reduction meta-task (`rgsproc`) from different entry points and to different end levels
    - extract source and background 1st and 2nd order spectra (`rgsspectrum`; run automatically through `rgsproc`)
    - create customized source lists or modifying existing EPIC source lists (`rgssources`) for scientific product extraction
    - produce plots of the dispersion versus cross-dispersion and energy versus dispersion planes, to verify the quality of the foreground and background extraction regions (`rgsimplot`).
    - generate a response matrix for a given source spectrum (`rgsrmfgen`)
    - create first- and second-order fluxed spectra (`rgsfluxer`)
  - with OM data
    - produce flat-fielded geometrically-corrected sky images for all lenticular filters, both for individual windows and for all windows combined, using image mode data
    - produce for individual windows and all windows combined, source lists, including color information for all lenticular filters using fast and image mode data
    - produce light curves time-series using fast mode data
    - produce tracking history information
    - extract wavelength and flux-calibrated OM grism spectra

- What SAS cannot do yet
  - create RGS exposure-corrected light curves

  - automatically create RGS spectra (and the corresponding response matrices) for extended sources

- Which PPS Data Products are available
  - EPIC
    * Exposure and observation images and image plots
    * Exposure maps and sensitivity images
    * Exposure and observation source lists
    * Calibrated and flagged event lists
    * Flare background time-series
    * HTML summaries
  - OM
    * Science window detector sky images and image plots
    * OM grism spectra
    * Observation source lists
    * Tracking star time series and history plots
    * Mosaiced filter-specific images and image plots
    * Fast Mode source time-series
    * HTML summaries
  - RGS
    * Spatial and energy-wavelength images and plots
    * Exposure maps
    * Calibrated and flagged event lists
    * Source lists
    * First- and second-order source and background spectra and spectral plots
    * Flare background time-series
    * First-order response matrices
    * HTML summaries
  - General
    * HTML ODF and PPS summaries
    * PPS script log, product indices
    * Calibration index files and attitude time series

Users are reminded that exposures with not scientific filters (*e.g.*: EPIC CAL_CLOSED, OM BLOCKED) are not intended to be processed by the PPS.